Engineering defect clustering in diamond-based materials for technological applications via quantum mechanical descriptors

Matúš Kaintz[®]* and Antonio Cammarata[®]†

Department of Control Engineering, Faculty of Electrical Engineering, Czech Technical University in Prague, Technicka 2, 16627 Prague 6, Czech Republic



(Received 2 October 2024; revised 24 January 2025; accepted 8 April 2025; published 12 May 2025)

Dopant-dopant and dopant-vacancy complexes in diamond can be exploited for the development of quantum computers, single-photon emitters, high-precision magnetic field sensing, and nanophotonic devices. While some dopant-vacancy complexes such as nitrogen- and silicon-vacancy centers are well studied, studies of other dopant and/or vacancy clusters are focused mainly on defect detection, with minimal investigation into their electronic features or how to tune their electronic and optical properties for specific applications. To this aim, we perform a thorough analysis of the coupled structural and electronic features of different dopant-dopant and dopant-vacancy cluster defects in diamond by means of first-principles calculations. We find that doping with p-type (n-type) dopant does not always lead to the creation of p-type (n-type) diamond structures, depending on the kind of cluster defect. We also identify the quantum mechanical descriptors that are most suitable to tune the electronic band gap about the Fermi level for each defect type. Finally, we propose how to choose suitable dopant atomic types, concentrations, and geometric environments to fabricate diamond-based materials for several technological applications such as electrodes, transparent conductive materials, intermediate-band photovoltaics, and multicolor emitters, among others.

DOI: 10.1103/PhysRevApplied.23.054029

I. INTRODUCTION

The unique set of extreme physical properties such as large thermal conductivity, carrier mobility, ultrawide band gap, high breakdown field strength, chemical inertness, and radiation hardness make diamond an ideal candidate material to reach for in demanding applications [1–5]. These applications include high-frequency FETs [6] and bipolar junction transistors (BJTs) [7], highpower high-frequency radio-signal amplification [8], highpower Schottky and PiN diodes [9–11], switches [1,3], inert electrodes [4], and radiation sensors [5]. Moreover, the qualities of diamond are of particular importance for both electric transmission and generation in future electric power systems. High-power switches and rectifiers [12] are essential for renewable-energy-dominated electrical grids, while the nuclear-fusion industry (e.g., UV photovoltaic cells [13] and nuclear-fuel production [14]) as well as solar photovoltaic cells [15,16] can benefit greatly

*Contact author: kaintmat@fel.cvut.cz †Contact author: cammaant@fel.cvut.cz

Published by the American Physical Society under the terms of the Creative Commons Attribution 4.0 International license. Further distribution of this work must maintain attribution to the author(s) and the published article's title, journal citation, and DOI. from diamond-based materials. To achieve the desired electronic or optical properties of diamond, it is necessary to tune its band gap about the Fermi level suitably. Depending on the specific application, we need to adjust the valence- and conduction-band edges or insert impurity bands into the band gap; the most common way to realize this is by introducing impurities (i.e., doping) into the pristine structure. Artificial diamond has been successfully doped in high concentrations by Al [17], B [18], and P [19], while doping with many other dopant atoms, such as Ge [20], Si [21], As [22], N [23], S [24], Mo, and W [25], has been experimentally proved to be feasible. Recently, significant attention has been paid to the color centers in diamond, mostly dopant-vacancy (X-V) complexes, as they seem crucial for the further development of quantum computers and single-photon emitters, as well as of high-precision magnetic field sensing, and nanophotonic, optomechanic, and plasmonic devices [26-34]. The color centers can be created during chemical vapor deposition and high-pressure high-temperature (HPHT) processes or by ion incorporation followed by thermal or HPHT annealing, depending on the dopant atomic type and desired application [21,26,28,35–37]. Other defects created by the aggregation of dopants and/or vacancies are dopants as nearest neighbors, dopants as next-nearest neighbors, and dopants aggregated around the vacancy, termed X-X, X- C_n -X, and X_n -V, respectively, where n corresponds to the number of carbon atoms between two dopants and dopants enclosing a vacancy [38–40]. All of these cluster defects containing nitrogen have been successfully created with suitable annealing conditions [40,41]. Moreover, clustering of impurities has been observed in systems doped with boron [42] or phosphorus [43], especially at high dopant concentrations. Studies focused on cluster defects other than X-V complexes are mostly dedicated to the calculation of defect formation and binding energies, to impurity levels, or to the different methods of defect detection in the sample [44–50]. In addition, the formation of cluster defects is often seen as unwanted [42] and their possible role in technological applications is overlooked.

In this context, we attempt to reveal coupled structuralelectronic features of different dopant and/or vacancy configurations and their effect on the band gap of diamondderived materials. We conduct a quantum mechanical investigation of diamond-based structures containing different types of cluster defects and dopant atoms in different concentrations. We suggest how to choose suitable dopant atomic types, concentrations, and kinds of aggregation to achieve the target electrical or optical effect. Finally, we discuss how the different cluster defects can be exploited in several technological applications, such as transparent conductive materials, laser diodes, intermediate-band (IB) photovoltaics, and multicolor emitters.

II. COMPUTATIONAL DETAILS

We conduct our simulations in the framework of the density-functional theory (DFT) with projectedaugmented-wave (PAW) pseudopotentials as implemented in the ABINIT software package [51–54]. According to previous studies [55,56], we select the Wu-Cohen form of the generalized gradient approximation (GGA-WC) energy functional [57] for all of our simulations, as it reproduces the lattice parameters and the width of the band gap of the pristine diamond with good agreement. The energy cutoff for the plane-wave basis set is chosen to be 1633 eV, with a corresponding 3265-eV cutoff for the PAW double grid. The sampling of the Brillouin zone is done within the Monkhorst-Pack scheme [58] and is scaled according to the size of the unit cell, by using a $21 \times 21 \times 21$ mesh for the pristine diamond and a $11 \times 11 \times 11$ mesh for the smallest doped structure. The self-consistent field is considered to achieve convergence when the energy difference between two subsequent iterations is below 10^{-11} eV. To obtain ground-state structural models, we perform geometry-optimization cycles until the largest component of the forces acting on the atoms is smaller than $2.5 \times$ 10^{-5} eV/Å. By using these settings, the geometry optimization of the pristine-diamond model yields a lattice parameter equal to 3.561 Å, which is consistent with the experimental value of 3.567 Å [55]. The calculated

band-gap size is 4.14 eV, in agreement with already reported DFT calculations [59]. Such a value is smaller than the experimental value of 5.47 eV as reported in previous studies [1,2]; indeed, it is known that DFT underestimates the band-gap width [60]. However, in the forthcoming discussion, we are interested in relative variations of the electronic features with respect to the ground-state model of the pristine-diamond structure; such relative variations are then not affected by the difference in the calculated band-gap value with respect to the experimental one. This has already been shown in a previous computational work [56], which compares the results obtained with different energy functionals, including the hybrid HSE06 [61–63]. For the same reasons, we conduct calculations without spin polarization. We are aware that band spin splitting occurs in the case of X-V complexes and in diamond-containing vacancies [64–66]. To assess potential differences between spin-polarized and nonpolarized calculations, we conduct benchmark spin-polarized calculations for a single concentration of the X-V defect (1.85%) with the spin magnetization set to 1.0 μ_B (S = 1/2). The results show that the geometry changes are minimal, as interatomic distances between dopants and neighboring carbons do not change by more than 0.01 Å. The most significant difference in the electronic structure is found in the systems in which the dopant and its neighboring carbon atoms form trigonal pyramidal configurations (see the B- and N-doped cases in Sec. III B). In these cases, the maximal shift in the position of the impurity bands is 0.3 eV, while for systems with an octahedral configuration (Al, P, Si) the shift is smaller, about 0.1 eV (see Table II). As we will see in the following discussion, these differences do not affect the overall trends that we are addressing. We perform calculations of defects in neutral charge states, although we acknowledge that defects can exist in their charged states. However, we emphasize that there is inherently no reason for such states to form in a sample doped exclusively with the considered defect and in the absence of external influences. Charged defects are likely to form when additional, often unintended, doping is present. For instance, Al- V^- and B- V^- defects may form in the presence of *n*-type impurities, such as single N or P atoms, in sufficient quantities. Similarly, external factors, such as applying voltage or light illumination, can induce charged defects [40,67,68]. Conversely, some charged defects, such as N-V- or Si-V-, are often desirable for applications in quantum computing or quantum sensing [30,40,69,70]. Similarly to spin polarization, we assume that X-V defects are prone to forming charged defects. This arises from their partially filled impurity bands as a result of the presence of dangling bonds. Furthermore, charged X-V defects are the most discussed charged defects in the literature, enabling validation of the results of our benchmark. The analysis of charged states is included in Sec. IIIB. As shown there, the observed

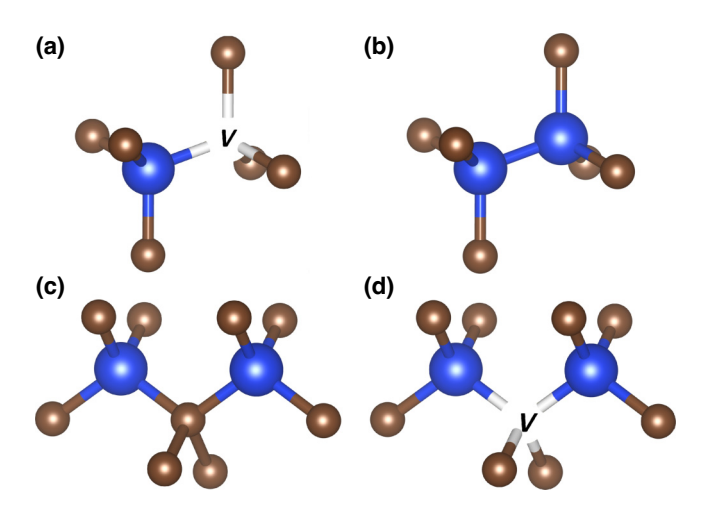


FIG. 1. A schematic showing the considered cluster defects: (a) X-V, (b) X-X, (c) X-C-X, and (d) X-V-X.

trends prove that adding and removing electrons from the defect affects the electronic features in a consistent way. Consequently, we do not anticipate deviations in the trends that we are addressing in our analysis when comparing equivalent charge states of different dopant atomic types.

In order to analyze how the introduction of the different cluster defects alters the electronic properties of the pristine diamond, we consider a large diversity of systems varying in dopant atomic type, concentration, and cluster-defect type. To consider both *electron acceptors* and *electron donors* (i.e., p- and n-type dopants, respectively), we choose five p-block atomic dopant types, namely, Al, B, N, P, and isovalent Si. However, as we shall see later in the discussion, when considering cluster defects, doping with p-type (n-type) dopant does not ensure the creation of a p-type (n-type) diamond structure. In order to create the model geometries representing different dopant concentrations, we first consider $2 \times 2 \times 2$, $3 \times 3 \times 3$, $4 \times 4 \times 4$,

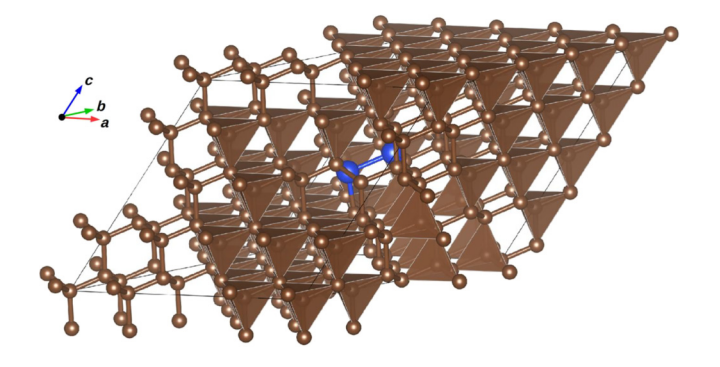


FIG. 2. An example of the primitive unit cell corresponding to the X-4-X-X system. The blue spheres represent the dopant atoms, while the brown spheres indicate the positions of the carbon atoms.

and $5 \times 5 \times 5$ supercells of the pristine-diamond structure, where one carbon atom is substituted with a dopant one; these geometries represent a dopant concentration equal to 6.25%, 1.85%, 0.78%, and 0.4%, respectively. For each of such models, we consider the following cases: (a) we remove one carbon next to the already substituted dopant, thus creating the X-V model structure, with a dopant and a vacancy as nearest neighbors [Fig. 1(a)]; (b) we substitute one carbon next to the dopant with a dopant of the same atomic type, thus creating the X-X model structure, with two dopant atoms as first neighbors [Fig. 1(b)]; and (c) we substitute one carbon that is in the second coordination sphere of the dopant with a dopant, thus creating the X-C-X model [Fig. 1(c)]. Moreover, after obtaining the relaxed geometries of the X-C-X models, we remove the carbon atom bonding with the two dopants, thus creating the X-V-X models [Fig. 1(d)], where a vacancy is introduced between two dopant atoms. We also consider diamonds solely with one vacancy as reference structures; we denote these model geometries using V. The atomic positions and lattice parameters of all the model geometries have been optimized and used to calculate the electronic properties discussed in the following sections. In what follows, we refer to the concentration of the defect as a whole, regardless the number of dopant atoms needed to form it; e.g., $5 \times 5 \times 5$ supercells, which are formed by 250 atoms, then represent a defect concentration equal to 1/250 = 0.4%. We term the generic models as Z-n-d, where Z is the atomic type of the dopant, n is the multiplicity of the supercell, and d is the defect type (d = X-V, X-X, X-C-X, X-V-X). For instance, the structure labeled as Al-4-X-X corresponds to a 128-atom supercell with two neighboring carbon atoms substituted by aluminum. An example of the primitive unit cell of the X-4-X-X system is shown in Fig. 2. We emphasize that to keep the computational load reasonable, we build the models by (i) assuming an ordered distribution of the defects and (ii) considering dopant concentrations that are not too low. However, we recall that the lowest concentrations considered here are achievable with a single-dopant defect (Al [17], B [18], and P [19]), and cluster defects are often formed naturally at high dopant concentrations [42,43]; this is supported by our formation- and binding-energy calculations reported in Sec. III. Moreover, as we will see, the features that we inspect in this work, such as the positions of the impurity electronic bands within the band gap and values of the quantum mechanical descriptors, do not change significantly when the concentration is reduced from 0.78% to 0.4%. Consequently, we may assume that these features would not change substantially with a further decrease in defect concentration. While it is true that experimental concentrations are often lower, we believe that a 0.4% concentration can adequately represent them without introducing significant inaccuracies to observed trends and values.

TABLE I. The defect formation and binding energies (electronvolts per defect) calculated for all systems with cluster defects. Single-dopant (X) and nondoped diamond with single-vacancy (V) energies are added for comparison.

	Defect formation energy E^f				Binding energy E^b			
	6.25%	1.85%	0.78%	0.4%	6.25%	1.85%	0.78%	0.4%
Al								
X	6.09	5.81	5.81	5.83				
X-V	2.73	4.58	4.86	4.93	-8.81	-7.45	-7.75	-7.97
X-X	6.46	8.69	9.13	9.26	-5.73	-2.93	-2.48	-2.41
X-C-X	6.36	9.57	10.00	10.14	-5.82	-2.06	-1.62	-1.52
X-V-X	4.73	7.21	7.24	7.22	-12.91	-10.64	-11.18	-11.52
В								
X	1.79	1.48	1.39	1.36				
X-V	4.61	5.30	5.48	5.55	-2.63	-2.40	-2.71	-2.88
X-X	2.19	2.22	2.20	2.19	-1.40	-0.75	-0.58	-0.53
X-C-X	2.09	2.35	2.37	2.38	-1.50	-0.61	-0.41	-0.34
X-V-X	2.86	4.16	4.18	4.17	-6.18	-5.03	-5.41	-5.63
N								
X	3.96	3.97	3.92	3.91				
X-V	5.70	5.90	6.05	6.11	-3.71	-4.30	-4.68	-4.87
X-X	3.67	3.65	3.56	3.53	-4.26	-4.30	-4.29	-4.29
X-C-X	6.64	5.93	6.84	6.81	-1.29	-2.02	-1.01	-1.01
X-V-X	5.02	4.98	4.99	4.99	-8.36	-9.18	-9.66	-9.91
P								
X	6.41	6.66	6.65	6.71				
X-V	4.62	5.04	5.13	5.17	-7.24	-7.85	-8.33	-8.61
X-X	12.02	13.77	13.96	14.12	-0.79	0.44	0.66	0.70
X-C-X	10.76	10.83	10.98	11.02	-2.05	-2.50	-2.32	-2.40
X-V-X	6.93	8.06	8.16	8.18	-11.34	-11.48	-11.94	-12.32
Si								
X	4.38	4.28	4.22	4.21				
X-V	4.04	5.22	5.51	5.64	-5.79	-5.29	-5.51	-5.64
X-X	10.20	11.08	11.06	11.05	1.44	2.51	2.62	2.64
X-C-X	6.59	8.05	8.09	8.11	-2.16	-0.52	-0.36	-0.30
X-V-X	6.52	8.13	8.21	8.22	-7.69	-6.65	-7.04	-7.26
V	5.45	6.22	6.80	7.07				

III. RESULTS AND DISCUSSION

In the following discussion, we will look at the different cluster-defect types separately. In the first subsection, we will describe the methods used in each type of analysis and we will examine the general features common to all defects. Then, we will investigate each defect type from the point of view of their geometry, and electronic structure, and, finally, we will consider different quantum mechanical descriptors and their effect on the band-gap size. We will see that in many cases, the geometric and electronic features depend on the atomic radii of the doping atoms. This is especially noticeable when we compare dopants from different periods of the periodic table. To make an easy distinction, we will refer to the period-2 elements B and N as *small-dopant atoms* and to the period-3 elements Al, Si, and P as *large-dopant atoms*.

To provide a preliminary guideline for the experimental synthesis of diamonds containing cluster defects, we calculate the formation energies for each considered

defect type, dopant atomic type, and concentration. While more comprehensive insights could be gained from phasediagram calculations at different temperatures and pressures, conducting these extensive simulations falls outside the scope of this study. Additional insight could also be obtained by scanning a broad range of defect configurations to identify the most probable structures under specific conditions. Such investigations often employ highthroughput approaches, Monte Carlo simulations, evolutionary algorithms, machine-learning models, or other techniques [71–74]. We point out that we calculate formation energies for supercells with optimized volume; this is because we believe that constant-volume calculations are not relevant for our study. Constant-volume calculations are commonly used when the formation energy is reported in the dilute limit, i.e., at concentrations at which no interactions exist between the defects. They are preferred in such cases because fixing the volume helps to more easily account for the so-called supercell error due to the elastic interactions between periodic images [75]. However, in our work, we report formation energies for each defect at every considered concentration without any extrapolation to the dilute limit. In fact, imposing a fixed volume would introduce unphysical strain and artificially inflate the formation energies, especially for systems representing high defect concentrations. On the other hand, for low concentrations, the changes of volumes are minimal. Moreover, our reported values clearly show that the formation energies tend to an asymptotic value as the concentration decreases. As a result, we can reasonably assume that the formation energies reported for a 0.4% concentration are close to those in the dilute limit. The formation energy [69,75–77] of a defect *D* is computed as

$$E^{f}[D] = E_{\text{tot}}[D] - E_{\text{tot}}[\text{bulk}] - \sum_{i} n_{i} \mu_{i}, \qquad (1)$$

where $E_{\text{tot}}[D]$ and $E_{\text{tot}}[\text{bulk}]$ denote the total energy of the defected structure and the total energy of the equivalent pristine-diamond supercell, respectively, and n_i is the number of atoms of type i removed $(n_i < 0, \text{ carbon})$ or added $(n_i > 0$, dopants) into the structure, while the μ_i values represent the corresponding chemical potentials, all obtained with the same simulation parameters. The references used for chemical potentials are as follows: (a) pure diamond (μ_C), (b) face-centered cubic aluminum (μ_{Al}), (c) α -rhombohedral boron (μ_B), (d) molecular nitrogen N₂ $(\mu_{\rm N})$, (e) black phosphorus $(\mu_{\rm P})$, and (f) the diamond lattice of silicon (μ_{Si}). We report the calculated formation energies in Table I. We observe relatively high formation energies in the cases in which two large dopants (Al. P, Si) are close to each other without the presence of a vacancy (the X-X and X-C-X systems). This is expected, as replacing two carbon atoms with large dopants significantly alters the bond lengths and induces local strain around the defect. Moreover, even single substitutional Al and P dopants yield formation energies between 5.8 and 6.7 eV, while both defects are often used in experiments [17,19]. We recall that diamond has been successfully synthesized with uniformly distributed impurities as large as Mo or W [25], which are significantly larger than the dopants considered in our study. In the case of the cluster defects, it is valuable to calculate the binding energy E^b [75] of the cluster defect D, as it provides an insight into whether defects prefer to remain isolated ($E^b > 0$) or combine to form cluster defects ($E^b < 0$). The binding energy is defined as follows:

$$E^{b}[D] = E^{f}[D] - nE^{f}[X] - mE^{f}[V],$$
 (2)

where n and m denote the number of dopants (1 or 2) and vacancies (0 or 1) in the defect, respectively, while $E^f[X]$ and $E^f[V]$ are the formation energies of a corresponding single substitutional dopant and a vacancy in the equivalent supercells, respectively.

We observe that the cluster formation energies are generally the lowest in the case of the highest defect concentration. We ascribe this to the interactions between the defects, as at high concentrations the cluster defects are in close proximity, which leads to binding interactions. This aligns with experimental observations showing that defect clustering predominantly occurs at high dopant concentrations [42,43]. In the case of small-dopant atoms (B, N), X-V-X defects exhibit lower formation and binding energies than X-V defects, consistently with the experimentally observed tendency of N atoms to cluster around vacancies [40]. For large-dopant atoms (Al, P, Si), X-V represents the most preferred configuration; in fact, the formation energy of X-V is, in general, even lower than that of X [78]. Moreover, for B and N, the X-X configuration is preferred over X-C-X, while, for larger dopants, the X-C-X configuration is favored, except when X = Al. This exception is probably caused by the atypical geometry of Al-X-X systems (Sec. III C). The binding energy is negative in nearly all cases, with the exception of P and Si in the X-X configuration; this suggests that the formation of these impurities may not be preferred. These findings are consistent with what has been reported in the literature [42,48,49].

A. Methodology and general features 1. Geometry analysis

The first step in our analysis is to investigate the influence of the defect on the geometry of the pristine structure. As expected, the introduction of a cluster defect reduces the number of symmetries compared to the pristine structure (space group $Fd\bar{3}m$, group number 227) and to the case of a single dopant coordinating a regular tetrahedron [point group T_d , Fig. 3(a)] of carbon atoms ($F\overline{4}3m$, no. 216) [56]; here, we will refer to the latter systems as "X" models. The only X structures with the lowest number of symmetries are those doped with nitrogen. In such geometries, the nitrogen atom is much closer to three carbon atoms than to the fourth, thus forming a trigonal pyramidal configuration $[C_{3v}, \text{ Fig. 3(b)}]$. Such systems possess the symmetries of the trigonal space group R3m (no. 160). We have observed that the environment of the same dopant is characterized by the same point group $(T_d \text{ or } C_{3v})$ irrespective of the concentration. The point group does not change even for the structures doped with the cluster defects. The only exception is the N-3-X-C-X system, as we will see in the following discussion.

2. Electronic structure analysis

We then proceed with the analysis of the electronic structure. As a first step, we need to establish a method for measuring the width of the band gap about the Fermi level. Usually, the band gap is measured as the energy difference between the conduction-band minimum (CBM) and the valence-band maximum (VBM); however, when numerous

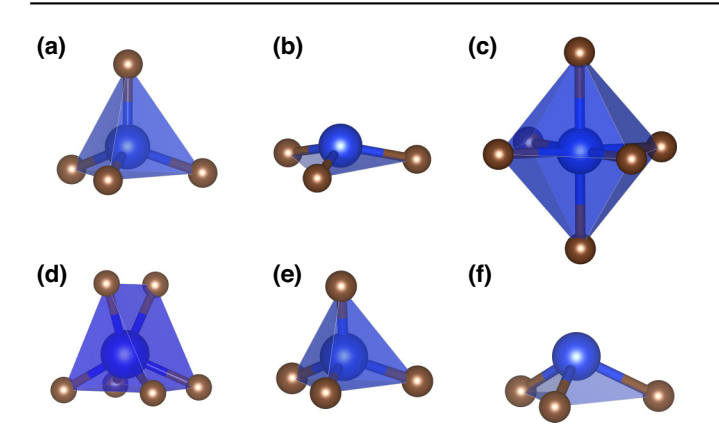


FIG. 3. A schematic representing all the coordination polyhedra found in the studied systems: (a) regular tetrahedron (T_d) , (b) trigonal pyramidal configuration (C_{3v}) , (c) distorted octahedron (D_{3d}) , (d) distorted trigonal prismatic configuration (C_{3v}) , (e) irregular tetrahedron (C_s) , and (f) irregular pyramidal configuration (C_s) .

highly localized intermediate bands (IBs) are present, the situation is much less straightforward. Adding defects to the structure can result in the creation of localized bands located below or above the Fermi level; the latter bands, when populated, represent trapped electrons that do not contribute to the *n*-type conductivity. To identify such bands, we calculate the *generalized inverse-participation ratio (IPR)* [79] by utilizing the projected density of states via

$$IPR(\epsilon) = \frac{\sum_{i=1}^{N} g(A_i, \epsilon)^2}{(\sum_{i=1}^{N} g(A_i, \epsilon))^2},$$
(3)

where $g(A_i, \epsilon)$ represents the density of states projected on the A_i atom-centered hydrogenlike orbitals and N is the number of atoms in the cell. In the forthcoming analysis, we will use the term valence band to refer to the occupied bands of the host matrix in the ground state and the term *impurity bands* to refer to the bands appearing due to the presence of the dopant. We will focus on the band gap that corresponds to the final electron jump to the conductive (delocalized) states in the conduction band, thus resulting in nonmetal-to-metal transition by means of n-type conductivity. Nevertheless, we recognize that the electron transition from the valence band to any localized band above the Fermi level results in the p-type conductivity, but this is not the focus of the present work [80]. Therefore, we measure the size of the band gap as the energy difference between the bottom of the conduction band and the localized IB with the highest energy that lies below it $(\Delta = \epsilon_{\text{CBM}} - \epsilon_{\text{IB}_{\text{max}}})$, as indicated in Fig. 4(a). According to this definition, the band-gap size is null in the case of the *n*-type degenerate semiconductors, as the Fermi level is located in the conduction band; thus, these materials

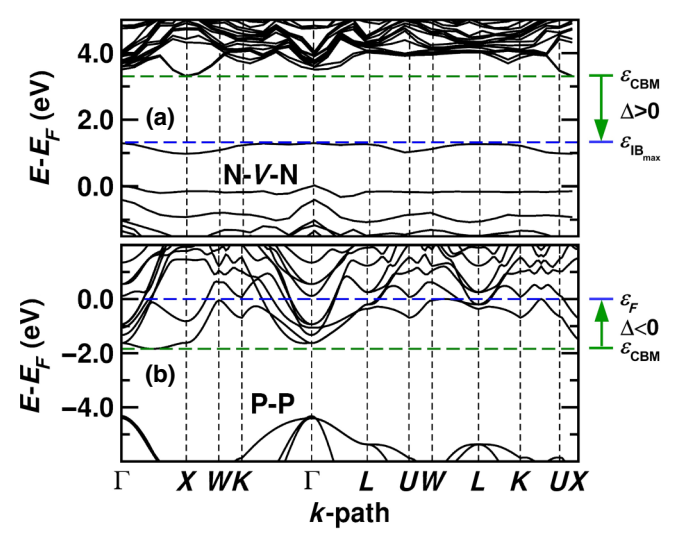


FIG. 4. A schematic demonstrating the method of measuring the band-gap width in this work. (a) The electronic band structure of the N-4-X-V-X system represents the vast majority of considered systems; the band gap is measured as a difference between the CBM ($\epsilon_{\rm CBM}$) and the intermediate localized band with the highest energy ($\epsilon_{\rm IB_{max}}$). (b) The band dispersion of the P-2-X-X indicates the method of measurement for degenerate n-type systems where the band gap is measured as the energy difference between the $\epsilon_{\rm CBM}$ and the Fermi level (ϵ_F) and is of negative value. The Fermi level is set to 0 eV.

show n-type metallic properties. To parametrize this situation consistently with our previous work [56], we use the definition of the generalized band gap. In the case of n-type degenerate semiconductors, we measure the band gap as an energy difference between the bottom of the conduction band and the Fermi level ($\Delta = \epsilon_{\text{CBM}} - \epsilon_F$), as shown in Fig. 4(b). As a result, negative values then represent the depth of the Fermi level in the conduction band. Due to this definition, we can analyze trends consistently with structures realizing positive band gaps. For clarity of the analysis, we will use the term *energy gap* we refer to any region in which no electron energy is allowed and the term *band gap* for the energy gap located below the bottom of the conduction band according to the definition mentioned above.

The electronic band structures are computed along the standard [81] piece-wise linear path joining the high-symmetry points in the irreducible Brillouin zone of the face-centered cubic lattice, regardless of the space group of the considered structure; we make this choice to aid the interested reader in the comparison with the previously studied diamond-doped systems with no cluster defects [56], where most of the considered systems have realized this kind of lattice. In the majority of the cases, we observe that the band-gap size decreases with the decrease in concentration, while a few exceptions can be found in the case

of X-V-X and X-C-X structures (see Sec. I in the Supplemental Material [82]). Such a deviation from the trend is caused either by a separation of the impurity band from the conduction band (B-, Si-X-V-X systems), thus forming a new IB, or by a change of geometry (N-3-X-C-X; see Sec. III D). Moreover, as expected, all doped systems show a narrower band gap than pristine-diamond structures.

3. General features of the electronic structure

In general, we observe that every defect type forms a degenerate semiconductor at least in the case of one dopant atomic type, mostly at higher concentrations. Furthermore, when we increase the concentration, we decrease the resemblance between the band structures of the clusterdefect systems and X-doped systems with the same defect concentration. This is especially true for the X-X and X-C-X defects, as well as for X-V structures doped with large dopants, the band structures of which resemble the X systems the most. In many cases, the band structure of the systems doped in the highest concentration (6.25%) of the defect does not resemble the band structure of the lower concentrations (1.85%, 0.78%, and 0.4%); this is expected, as the distance between the defects in the former case is short enough and defects cannot be considered as isolated. We observe that the evolution of the band structure with gradually decreasing concentration can be summarized as the following path: (a) a degenerate semiconductor of p-type; (b) the Fermi level moves toward the VBM; (c) the Fermi level is in the valence band near the VBM; and (d) a split of the band(s) formed by dopant states from the valence band. The process is similar in the case of n-type semiconductor; the only difference is that the Fermi level moves to the bottom of the conduction band and the separation is from the conduction band. If the system is a degenerate semiconductor and no energy gap exists in the band structure at high concentration, we can distinguish whether the semiconductor will follow the path of p- or n-type semiconductor presented above by analyzing the curvature of the bands that are crossed by the Fermi level. If we observe a negative (concave) curvature of these bands at Γ , the semiconductor will follow the p-type path when the concentration is decreased.

We continue our analysis by considering the projected density of states (PDOS). The first thing we note is that irrespective of the type of dopant, concentration, or defect type, the p_x and p_y orbitals centered at each atomic site are degenerate. The states around the Fermi level are added to the pristine band structure mostly by dopants and their first neighbors, which suggests hybridization of their orbitals. After a defect is created, additional states are added to the top of the valence band, the bottom of the conduction band, or into the former band gap, thus creating separated localized bands or any combinations of these options. The

dopant atomic type and the kind of defect determine the position of the dopant states in a nontrivial way; however, we can identify some general trends. When X-V structures are doped with dopants with large atomic radii (Al, P, Si), the top of the valence band and the bottom of the conduction bands show a d- and s-orbital-like character, respectively [Fig. 5(a)]. We ascribe this behavior to the octahedral configuration of the dopant with its neighbors: as four carbon neighbors lie on a plane containing a dopant, the d orbitals represent the best approximation of the electron density at the dopant site. By analyzing the PDOSs of the X-C-X systems, we observe that the bridging carbon located between the two dopants acts more as a different type of dopant than as the neighbors or dopants of the other dopants themselves. In fact, together with the dopants, it contributes to the majority of the states around the Fermi level; in degenerate p-type semiconductors, the energy levels above the Fermi level but still in the valence band are almost solely formed by the

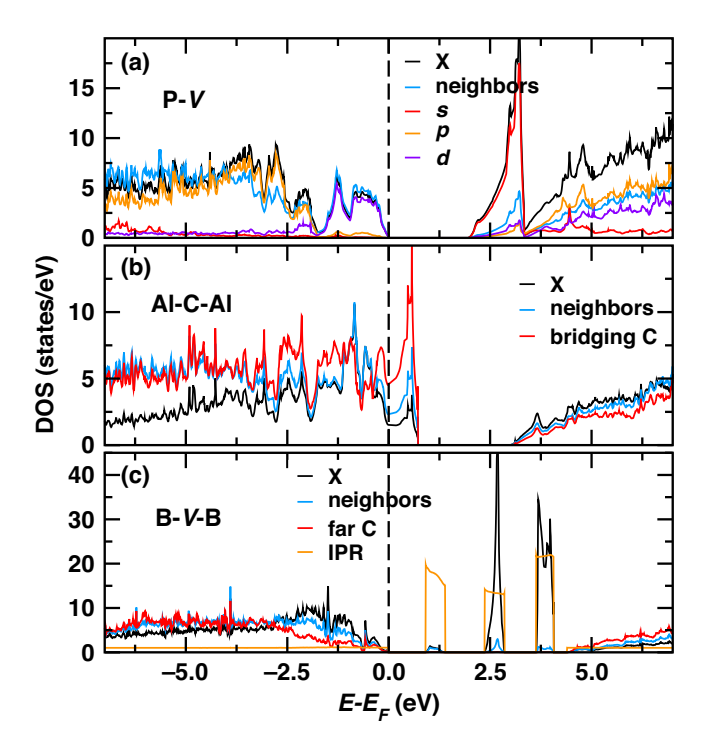


FIG. 5. The projected density of states (PDOS) of the (a) P-3-X-V, (b) Al-3-X-C-X, and (c) B-4-X-V-X systems. The "X," "neighbors," "bridging C," and "far C" labels correspond to the projections onto the dopant atoms, the dopant neighbors, the bridging carbon between dopants in the X-C-X structure, and carbon far from the defect, respectively. The labels "s," "p," and "d" in (a) represent the orbitals centered at the dopant atomic site. The *inverse-participation ratio* (*IPR*) value is equal to one for completely delocalized states, while for maximally localized states the IPR equals the number of atoms in the unit cell (127). The values of dopants and neighbors are normalized according to their number in the system.

states of this carbon [Fig. 5(b)]. Therefore, we can conclude that the bridging carbon in X-C-X systems plays a major role in forming degenerate semiconductors. The other notable PDOSs correspond to the X-V-X systems. As we will see, the X-V-X structures feature many highly localized intermediate states. Therefore, these states are nearly solely contributed by the dopant atoms; to emphasize this, we report the PDOS of the B-4-X-V-X system together with the corresponding IPR in Fig. 5(c) as an example.

4. How to engineer the width and character of the band gap

Here, we recall that we measure the size of the band gap as the minimum energy needed to achieve *n*-type conductivity. In our previous research [56], we have observed the dependence of the size of the band gap on the X—C interatomic distance, as it determines the degree of orbital hybridization between the dopant and the surrounding carbon atoms. Here, we shall see that such a clear relation no longer exists; however, the atomic radii and X—C distances still affect the local distributions of the electronic density in various ways. We then proceed by analyzing each defect type separately in the following way. We start by considering more general descriptors such as Hirshfeld atom charges [83] and bond covalencies [84], the latter defined in terms of the atom-projected density of states; subsequently, to dive even into more detail, we analyze the local distribution of the electronic density by means of the orbital-polarization descriptor [85–88]. The orbital polarization $\mathcal{P}_{i,j}(A,B)$ is defined as

$$\mathcal{P}'_{i,j}(A,B) = \frac{n_i(A) - n_j(B)}{n_i(A) + n_i(B)},\tag{4}$$

where $n_i(A)$ and $n_j(B)$ are the occupancies of the i and j set of atomic orbitals centered on atoms A and B, respectively. Due to this definition, $\mathcal{P}'_{i,j}(A,B)$ is an effective and convenient way to measure the excess of charge in the i orbital relative to the j orbital. To simplify the notation, we will use the symbol $\mathcal{P}'_{i,j}(A)$ when comparing the charge in the orbitals of the same atom (A=B). We adopt atom-centered hydrogenlike wave functions to calculate the orbital polarizations at the site of the substituents and the neighboring carbon atoms. With this approach, we partition the electronic density according to the spatial character of the orbital and examine the possible preferential charge distributions in the local environment of the dopant. Since the p_x and p_y orbitals are degenerate, it is sufficient to consider $\mathcal{P}_{p_x,p_z}(X)$ (= $\mathcal{P}_{p_y,p_z}(X)$) and $\mathcal{P}_{p_x,p_z}(C)$ (= $\mathcal{P}_{p_y,p_z}(C)$) in our analysis, as $\mathcal{P}_{p_x,p_y}(X) = \mathcal{P}_{p_x,p_y}(C) = 0$.

Finally, we compare the relative occupation of the p_x (= p_y) and p_z orbitals of the dopant and the surrounding carbon atoms. In this way, we obtain details about the spatial distribution of the charge along the bond axis. As it

would be too dispersive to treat each carbon neighbor and dopant separately, we will rely on the average values of the descriptors for neighbors and dopants, unless specified otherwise. The average orbital polarization $\mathcal{P}_{i,j}(A,B)$ is calculated as follows:

$$\mathcal{P}_{i,j}(A,B) = \frac{\sum_{p=1}^{s_A} n_i(A_p)/s_A - \sum_{p=1}^{s_B} n_j(B_p)/s_B}{\sum_{p=1}^{s_A} n_i(A_p)/s_A + \sum_{p=1}^{s_B} n_j(B_p)/s_B}, \quad (5)$$

where s_A and s_B are the numbers of atoms of the A (in our case, dopants) and B (neighbors) kinds, respectively. The average values of the covalency $C_{X,C}$, Hirshfeld charges $\mathcal{H}(A)$, and polarizations of the same atoms $(\mathcal{P}_{i,j}(A))$ are calculated as arithmetic means:

$$\mathcal{P}_{i,j}(A) = \frac{1}{s_A} \sum_{p=1}^{s_A} \mathcal{P}'_{i,j}(A_p), \tag{6}$$

$$C_{X,C} = \frac{1}{s_A} \left(\sum_{p=1}^{s_{A_1}} C'_{X_1,C_p} + \sum_{p=1}^{s_{A_2}} C'_{X_2,C_p} \right), \quad (7)$$

$$\mathcal{H}(A) = \frac{1}{s_A} \sum_{p=1}^{s_A} \mathcal{H}'(A_p), \tag{8}$$

where s_A is the number of atoms A (neighbors or dopants), the X—C bond covalency $(C_{X,C})$ is calculated between each dopant $(X_1 \text{ or } X_2)$, and all their respective neighbors (s_{A_1}, s_{A_2}) separately and then averaged by the number of all neighbors (s_A) . $\mathcal{P}'_{i,j}(A)$ and $\mathcal{H}'(A)$ always correspond to the orbital polarizations considering the i and j orbitals and the Hirshfeld charge on the single atom A, respectively, while $C'_{X,C}$ represents the covalency of the single bond between two atoms, X and C.

B. X-V defect

1. Geometry analysis

Structures with an X-V defect [Fig. 1(a)] can be split into two groups according to the local environment of the dopant: structures doped with atomic types with large atomic radii (Al, Si, P) and small radii (B, N). During the relaxation procedure, dopants with large radii migrate from the initial position in such a way that they eventually create distorted octahedra formed by six neighboring carbon atoms $[D_{3d}; \text{ Fig. 3(c)}]$, effectively suppressing the vacancy from the structure. This configuration is often called the split-vacancy configuration and is commonly formed in the case of impurities with large atomic radii [28,89]. The regular octahedral environment allows us to realize the symmetries of the trigonal space group $R\bar{3}m$ (no. 166). Systems with small radii dopants preserve the existence of the vacancy next to the dopant, thus creating a trigonal pyramidal configuration [C_{3v} ; Fig. 3(b)]. These systems realize a

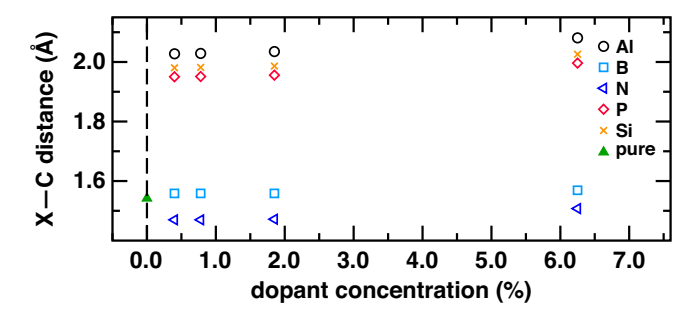


FIG. 6. The interatomic distance between the dopant atom and the carbon neighbors in its first coordination shell as a function of the dopant concentration.

trigonal space group but with a reduced number of symmetries compared to the previous case (R3m, no. 160). Interestingly, we observe that the increase in the multiplicity of the cell, i.e., decreasing the defect concentration, decreases the X—C distances at fixed dopant atomic type (Fig. 6).

2. Electronic structure analysis

We begin by considering X-V models doped with large-dopant atoms (Al, Si, P); we recall that dopants in these structures coordinate carbon octahedra [Fig. 3(c)]. At all concentrations, we observe that all the systems display behavior as in p-type doping, despite P and N being electron donors [see Figs. 8(c)–8(d)]; an exception is found for the B-, P-2-X-V models, which do not have any band gap. On the other hand, the band structures of the systems doped with Al and Si show a resemblance to the X

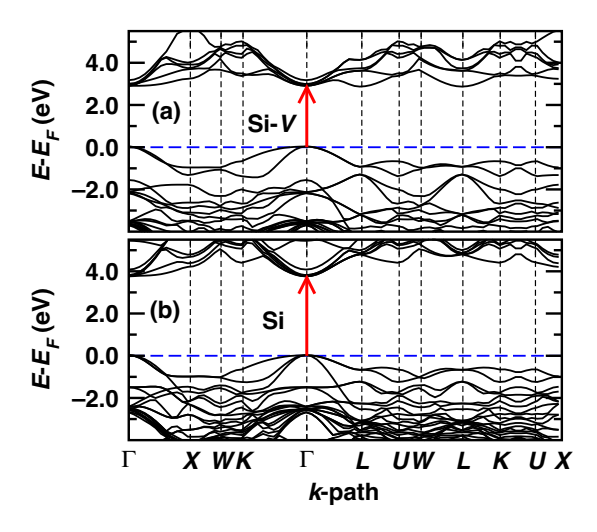


FIG. 7. The electronic band structures of the (a) Si-3-X-V and (b) Si-3-X systems. The red arrow connects k-points corresponding to the minimal-energy transition to the conduction band. The Fermi level is set to 0 eV.

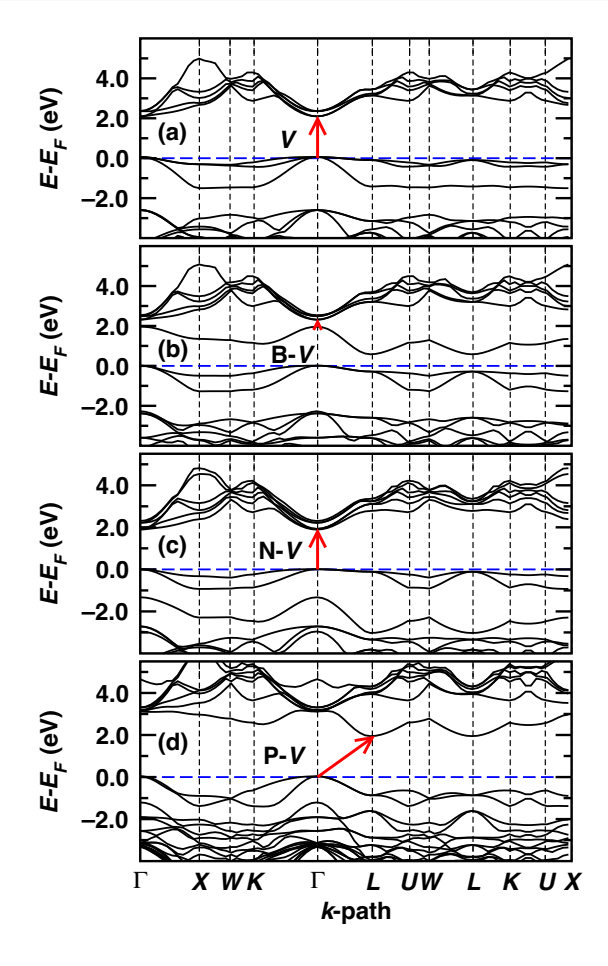


FIG. 8. The electronic band structures of the (a) V-3-X, (b) B-3-X-V, (c) N-3-X-V, and (d) P-3-X-V systems. The red arrow connects k-points corresponding to the minimal-energy transition to the conduction band. The Fermi level is set to 0 eV.

structures doped with the same dopant but with a narrower band gap (Fig. 7). The band structures of the second group, doped with B and N, which preserve the presence of the vacancy [Fig. 3(b)], are similar to the band structure of diamond, which contains a sole vacancy. As shown in Figs. 8(a)–8(c), the presence of a vacancy induces the formation of IB(s) in the band gap of the pristine diamond. The most significant difference between the B-X-V [Fig. 8(b)] and N-X-V [Fig. 8(c)] systems is the position of one of the impurity bands; in the B-doped case, this band is above the Fermi level, while in the N-doped case, it is below the Fermi level. The same holds for all considered concentrations. The positions of the calculated IBs are comparable with those reported in the literature (e.g., Al-X-V [90], B-X-V [44], and N-X-V [64,91]).

3. Charged states

To evaluate the influence of charge states on the positions of the impurity bands within the band gap, we

perform a study of charged X-V defects in 1.85% concentration. The charges considered span from completely empty to completely filled impurity bands closest to the Fermi level within the band gap. For instance, the N-X-V defect introduces two closely packed bands in the middle of the band gap, which together can accommodate up to four electrons. In the neutral state, these bands are occupied by a single electron; thus, we consider charge states of +1, 0, -1, -2, and -3. The charge states and assigned spin states are consistent with computational and experimental studies on various X-V defects (Al [90], B [69], N [40], P [92], and Si [30]), although many studies do not consider highly charged states such as -3. Such highcharge states are unlikely to form; nevertheless, they are useful for observing trends in the change of positions of impurity bands.

In all five cases, removal of electrons from the defect shifts impurity bands toward lower energies, while adding electrons shifts the bands to higher energies. The only exception is positively charged silicon, where the bandgap changes are negligible. However, this trend is not always apparent from Table II due to the method of our band-gap measurement. Negatively charged B-X-V defects have the uppermost band already merged with the CBM, leading to a sudden increase in the band-gap size. This happens because now the band gap is measured as an energy difference between the CBM and the top of the second IB, closer to the valence band [see Fig. 8(b)]. Similarly, P-X-V seemingly even exhibits an opposite trend; this is due to the fact that one of the impurity bands is merged with the CBM

TABLE II. The generalized band-gap values (eV) of X-V defects at 1.85% concentration in different charge states. The spin state of each defect is reported in the second row below the band-gap size. The labels "D" and "M" denote cases in which one of the IBs has detached from or merged with the conduction band, leading to abrupt changes in the band-gap size. The first row corresponds to the neutral defects without spin polarization, as considered in our analysis.

Charge	Al	В	N	P	Si
0 (S = 0)	2.53	0.35	1.89	1.91	2.84
3				0.20	
				D 0	
2				0.14	2.66
				D 1/2	0
1	2.67	0.60	2.32	1.69	2.69
	0	0	0	1	1/2
0	2.42	0.32	1.60	1.85	2.71
	1/2	1/2	1/2	1/2	1
-1	2.11	0.86	0.73	2.08	2.59
	1	M 1	1	0	1/2
-2	1.94	0.67	0.48		2.42
	1/2	M 1/2	1/2		0
-3	1.75	0.47	0.25		
	0	M 0	0		

in the neutral state, as this band moves toward lower energies, the band gap narrows [see Fig. 8(d)]. This band fully detaches from the CBM once the charge is higher than +1, which results in a significant drop in the band-gap width. With these considerations, the changes in impurity-band energies with respect to changes in charge states are evident. The intended formation of the charged defects can then serve as one of the techniques to tune the band-gap size and the positions of the impurity bands.

4. How to engineer the width of the band gap

We begin our analysis of the X-V systems by considering how the concentration of the defect affects the band-gap size. In the case of all cluster defects, we observe that the interval that characterizes the spread of the bandgap values for the same dopant atoms with the change of concentration is significantly larger than in the case of structures doped with a single dopant (X). This is because the drop of the band-gap size between 1.85% and 6.25% concentration is enormous (up to 2 eV) in the case of cluster defects. At such a high defect concentration, wide impurity bands fill nearly the whole pristine band gap, thus reducing its size, or even closing the gap completely. For this reason, we believe it is more descriptive to report the spread of the band-gap values for the same atom with 6.25% concentration neglected. In the X-V systems, the spread of the energy values is no more than 0.6 eV, with one exception being phosphorus, when we consider only lower concentrations than 6.25%. This value is very similar to the X systems.

We continue by examining the Hirshfeld charges of the dopant and neighboring atoms (Fig. 9). The Hirshfeld charges of the large-dopant atoms (Al, P, Si) and their neighbors depend on the atomic radius of the dopant; the value of the charge increases at decreasing radius. Moreover, systems with narrower band gaps (B, N) exhibit the largest absolute values of the Hirshfeld charges of the neighbors [Fig. 9(a)] and the smallest for the dopant [Fig. 9(b)]. We recall that smaller dopants preserve the vacancy, while larger atoms form an octahedral configuration. Therefore, it seems that there is a connection between the values of the Hirshfeld charge and the coordination environment of the dopant. Similarly, the dopant-neighbor bond covalencies $C_{X,C}$ depend on the atomic radii of the larger dopant atoms but we do not observe any visible general trend for the band-gap size as a function of the covalency (Fig. 10). However, when we compare dopants with the same local environments (D_{3d} or C_{3v}), we can see that the band-gap size tends to increase with larger covalency values. Moreover, we recognize that the covalency value increases with decreasing concentration; the opposite trend has been found for the structures with X defect [56]. This can be ascribed to the fact that the X—C distances in the X-V systems decrease with decreasing concentration,

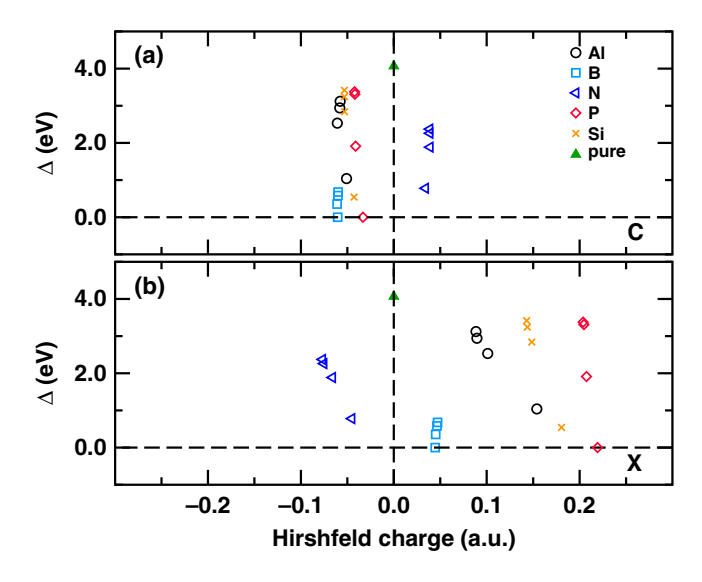


FIG. 9. The generalized band gap as a function of the Hirshfeld charges of (a) the dopant first neighbors and (b) the dopant in the X-V systems.

while the opposite is true for X systems, thus determining the degree of orbital hybridization and therefore the bond covalency. Furthermore, the n-type doped systems show the largest covalency values, consistently with the X models. This shows us that even when the n-type dopants create p-type structures when clustered with vacancy, they still preserve more covalent bonds with carbon neighbors than p-type dopants. Nevertheless, we observe that the covalency values are lower for every dopant when compared to X structures.

As expected, structures that preserve the existence of the vacancy [trigonal pyramidal configuration; Fig. 3(b)] display higher absolute $\mathcal{P}_{p_x,p_z}(C)$ and $\mathcal{P}_{p_x,p_z}(X)$ values due to the distorted environment around the dopant (Fig. 11). This is especially visible for $\mathcal{P}_{p_x,p_z}(X)$, where structures with octahedral configuration show values that are lower by one order of magnitude. Moreover, the $\mathcal{P}_{p_x,p_z}(X)$ values depend on the radius of the large atoms, while they do not change significantly with the change of concentration.

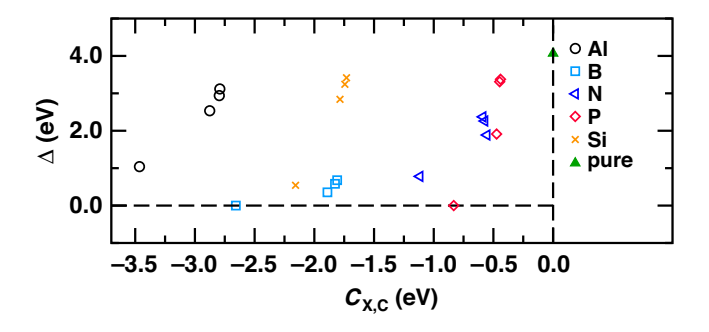


FIG. 10. The generalized band gap as a function of the X—C bond covalency $C_{X,C}$ in the X-V systems.

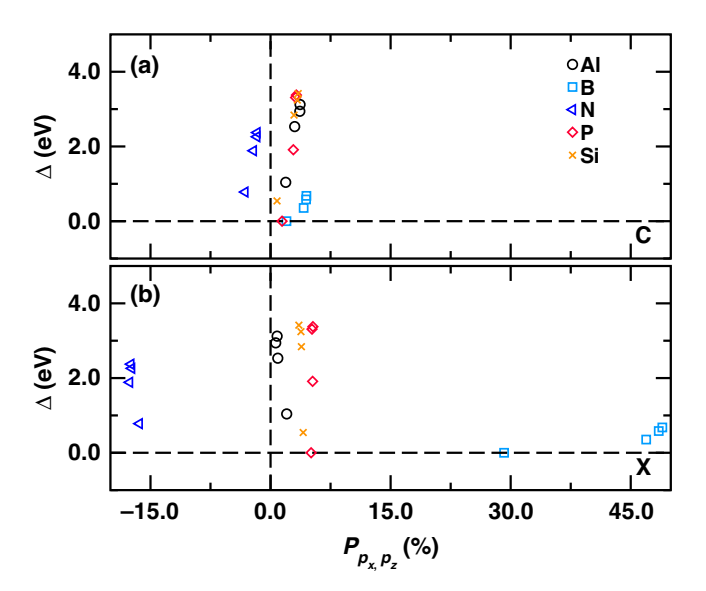


FIG. 11. The generalized band gap as a function of (a) $\mathcal{P}_{p_x,p_z}(C)$ and (b) $\mathcal{P}_{p_x,p_z}(X)$ in the X-V systems.

Since the large absolute $\mathcal{P}_{p_x,p_z}(X)$ values mean a smaller band-gap size, the narrow band gaps can be achieved by doping with dopants that form a trigonal pyramidal configuration, i.e., dopants with small radii (B, N). B-doped structures display a narrower band gap and positive values of $\mathcal{P}_{p_x,p_z}(X)$, while N-doped systems show a wider band gap and negative $\mathcal{P}_{p_x,p_z}(X)$. Therefore, it seems that the number of valence electrons is crucial in determining the size of the band gap in the case of small dopants even when all dopants create p-type diamonds. Finally, we do not observe any regular trend of the band-gap size as a

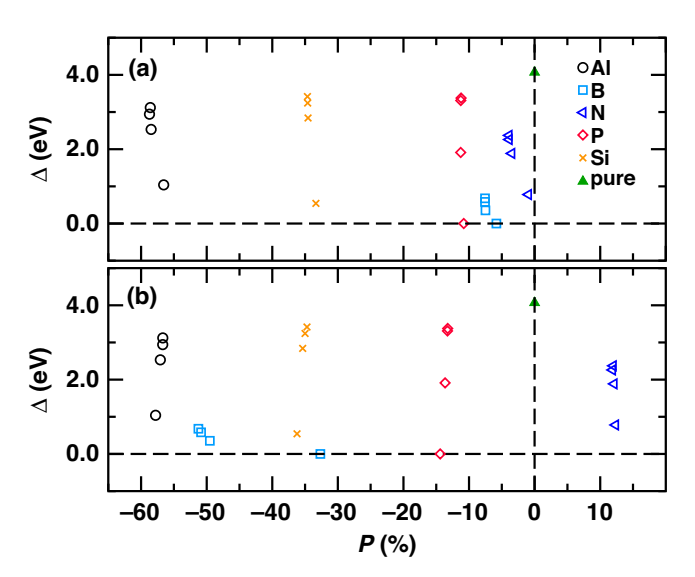


FIG. 12. The generalized band gap as a function of (a) $\mathcal{P}_{p_x,p_x}(X, C)$ and (b) $\mathcal{P}_{p_z,p_z}(X, C)$ in the X-V systems.

function of $\mathcal{P}_{p_z,p_z}(X, C)$ (Fig. 12), while $\mathcal{P}_{p_x,p_x}(X, C)$ values closer to zero correspond to structures with a trigonal pyramidal configuration and, therefore, a smaller band gap.

In summary, dopants with small atomic radii realize significantly narrower band gaps while showing larger dopant polarizations $\mathcal{P}_{p_x,p_z}(X)$ by one order of magnitude. When considering p-type dopants, we can order the dopant coordination numbers (CNs) with respect to the size of the band gap from the largest to smallest as follows: tetrahedral [CN = 4, Fig. 3(a)], octahedral [CN = 6; Fig. 3(c)], and trigonal pyramidal [CN = 3; Fig. 3(b)] dopant coordinations. Moreover, in the case of octahedral coordination, the values of $C_{X,C}$, $\mathcal{P}_{p_x,p_z}(X)$, $\mathcal{P}_{p_x,p_x}(X,C)$, and $\mathcal{P}_{p_z,p_z}(X,C)$, as well as Hirshfeld charges of the dopant and its neighboring atoms, depend on the atomic radii of the dopants. In the case of smaller atoms, the number of electrons (electron acceptor versus donor) seems to have a more important role in affecting the values of such physical descriptors.

C. X-X defect

1. Geometry analysis

In the structures with an X-X type of defect [Fig. 1(b)], each dopant coordinates three carbon atoms in a trigonal pyramidal coordination environment $[C_{3v}, Fig. 3(b)]$. In general, the geometric environments of each of the two X dopants are very similar; the only exceptions are represented by the structures doped with aluminum, where one of the dopants has six carbon neighbors [Fig. 3(d)] and the X—X distance is as large as approximately 2.2 Å. We observe that in all cases, the X—C distances are smaller than the X—X distances. This is especially significant in the case of dopants with small atomic radii, where the difference between the X—C and X—X distances is approximately 0.4 Å for boron and approximately 0.7 Å for nitrogen. The structures realize the symmetries of the trigonal space groups $R\bar{3}m$ (no. 166) or $R\bar{3}m$ (no. 160), according to whether or not the local environments of the two dopants are identical, respectively.

2. Electronic structure analysis

X-X systems doped with Al, P or Si (large atomic radii) show band structures that resemble those of the X models the most (see Sec. II in the Supplemental Material [82]). The structures doped with P are degenerate *n*-type semiconductors, like the corresponding X-doped structure, while systems doped with Al and Si display a narrower band gap when compared to their X-doped equivalents. However, even if the Al-X-X and Al-X band structures are very similar, the major difference is in the electron occupation of the impurity bands. The Al-X-X systems exhibit a fully occupied impurity band near the valence band; thus it cannot contribute to the *p*-type conductivity and the systems behave as *intrinsic* (*i*-type) semiconductors. Similarly, systems doped with N show *i*-type behavior, as the

N atoms contribute with very deep fully occupied donor states closer to the valence band than to the conduction band, consistently with other studies [93]. Moreover, the B-doped systems are either a degenerate *p*-type semiconductor or form an empty acceptor IB 0.7 eV above the Fermi level at the lowest concentration of the defect. This is a well-known feature when the clustering of boron atoms in diamond reduces the conductivity [42].

3. How to engineer the width of the band gap

We recall a method of band gap measurement for degenerate *n*-type semiconductors that we defined in Sec. III A. The generalized band gap is measured as an energy difference between the bottom of the conduction band and the Fermi level ($\Delta = \epsilon_{\rm CBM} - \epsilon_F$). As a result, negative values represent the depth of the Fermi level in the conduction band. In X-X systems, both dopants are in very similar or equal coordination environments, resulting in nearly equal values of descriptors such as the X—C bond covalency and polarizations. The only exceptions are the Al-doped systems, where one of the dopants is close to six carbon atoms instead of three [Fig. 3(d)], while the second dopant is in an expected trigonal pyramidal environment [Fig. 3(b)], similar to the other X-X structures. Moreover, the band structures and density of states of all X-X defects are the most similar to the structures with just one dopant. The spread of the band-gap sizes with fixed atomic types for different concentrations varies noticeably more than it does for X systems. The width of this interval is 1.1 eV when we neglect 6.25% concentration. We observe that the highest absolute (positive and negative) values of the dopant Hirshfeld charges correspond to the n-type dopants [Fig. 13(b)]. Furthermore, it seems that the increase in the Hirshfeld charges of the neighbors [Fig. 13(a)] decreases the band-gap size of the systems with positive band gaps (all systems except P-doped). A very similar trend can be found when we inspect the plot of dopant-carbon bond covalency $C_{X,C}$ (Fig. 14). Increasing $C_{\rm X,C}$ decreases the positive band-gap width, while Aldoped systems are very slightly off the trend. However, we need to take into account the fact that Al-doped systems are the only ones with nonregular geometry; in fact, the presented covalency value is an average of very high (dopant with six neighbors) and relatively low (dopant with three neighbors) covalency values. Even in the case of X-X structures, we can distinguish a covalency threshold that acts as a boundary between p- and n-type doped structures. Moreover, if we neglect Al-2-X-C-X, the difference between the p- and n-type covalencies is of significant size (0.6 eV).

We proceed by considering the orbital polarizations of the dopant $\mathcal{P}_{p_x,p_z}(X)$ and surrounding carbons $\mathcal{P}_{p_x,p_z}(C)$, as shown in Fig. 15. In both cases, an increase in the polarization seems to decrease the size of the band gap

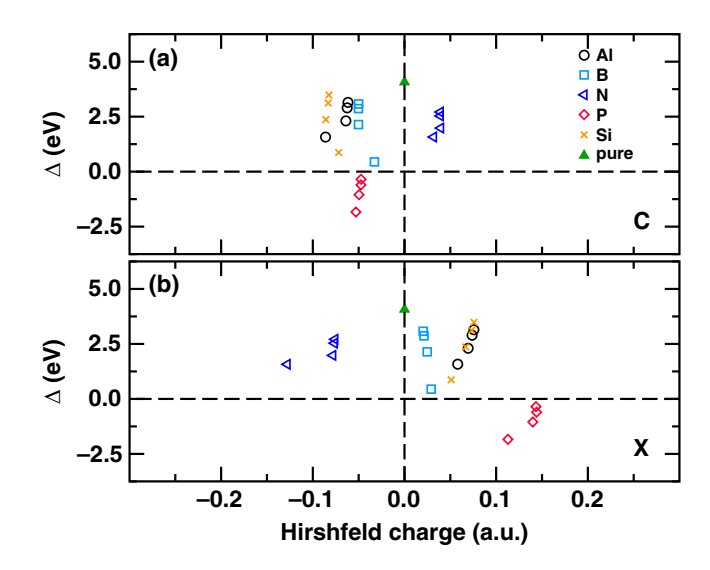


FIG. 13. The generalized band gap as a function of the Hirsh-feld charges of (a) the first neighbors of the dopants and (b) the dopant in the X-X systems.

when p-type systems and Si are considered. Second, n-type dopants show $\mathcal{P}_{p_x,p_z}(C)$ values close to zero and only negative $\mathcal{P}_{p_x,p_z}(X)$. The n-type dopants exhibit the highest $\mathcal{P}_{p_x,p_z}(X,C)$ and $\mathcal{P}_{p_z,p_z}(X,C)$ values, while they are the only cases realizing positive $\mathcal{P}_{p_z,p_z}(X,C)$ (Fig. 16). On the other hand, we do not see any regular trend with the increase of charge at the atomic dopant side of the bond (increase of $\mathcal{P}_{p_x,p_x}(X,C)$ and $\mathcal{P}_{p_z,p_z}(X,C)$) as the band-gap width of the B-doped structures is reduced more significantly by introducing the second dopant.

In summary, by realizing an X-X clustering defect, we can still create *p*- and *n*-type structures by doping with *p*- and *n*-type dopants. We have noted that adding the second dopant reduces the band-gap size of *p*-type and Si-doped structures when compared to the single-dopant case; adding the second phosphorus preserves the *n*-type degenerate properties while keeping the depth of the Fermi level in the conduction band nearly unchanged. On the other hand, donor states in the nitrogen-doped systems are now much deeper, i.e., much closer to the valence band

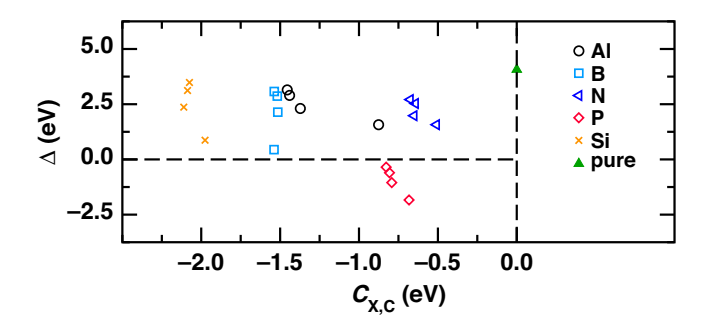


FIG. 14. The generalized band gap as a function of the X—C bond covalency $C_{X,C}$ in the X-X systems.

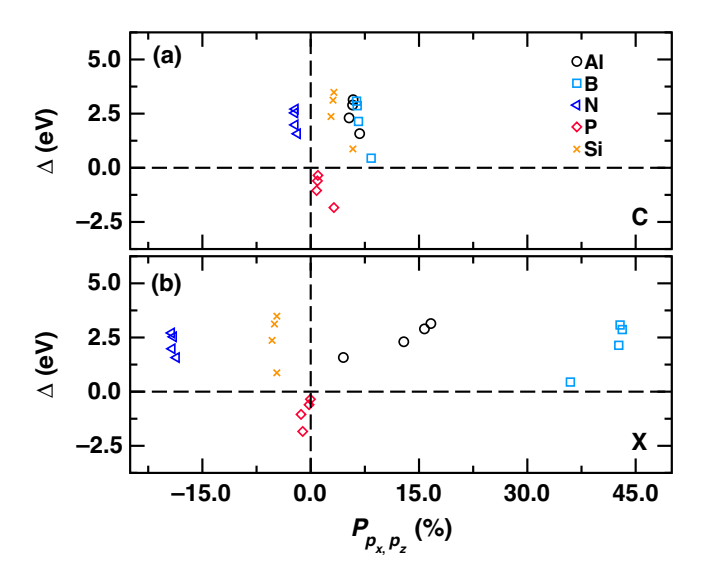


FIG. 15. The generalized band gap as a function of (a) P_{p_x,p_z} (C) and (b) P_{p_x,p_z} (X) in the X-X systems.

than to the conduction band. Moreover, we have seen that an increase in $\mathcal{P}_{p_x,p_z}(X)$, $\mathcal{P}_{p_x,p_z}(C)$, or $C_{X,C}$ decreases the band-gap width of the p-type and Si systems.

D. X-C-X defect

1. Geometry analysis

Regarding the X-C-X defect type [Fig. 1(c)], the number of symmetries depends on the similarity of the local environments of the two dopants: when the X—C distances about one dopant are the same as about the other dopant, the number of symmetries possessed by the structure is higher than in the case of a set of dissimilar distances. In general, this is true for all the kinds of defects that

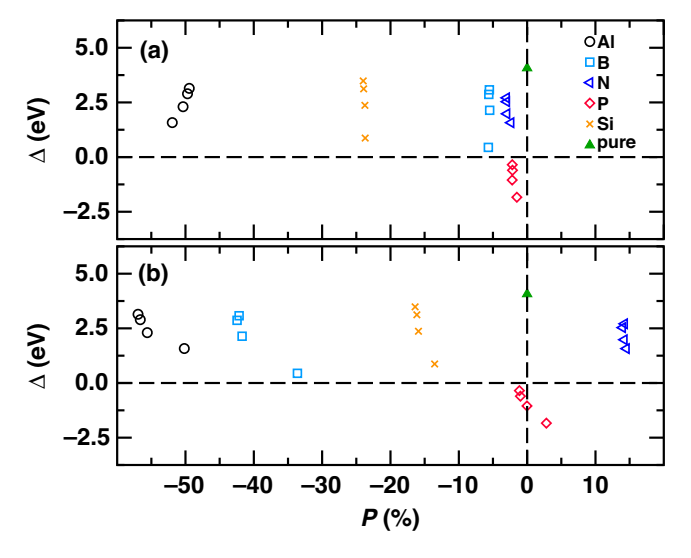


FIG. 16. The generalized band gap as a function of (a) $\mathcal{P}_{p_x,p_x}(X, C)$ and (b) $\mathcal{P}_{p_z,p_z}(X, C)$ in the X-X systems.

contain two dopants. The local environments of the two dopants in the X-C-X systems are very similar irrespective of the dopant atomic type and form irregular tetrahedrons with their neighbors $[C_s; Fig. 3(e)]$, except for nitrogen doping. In this case, one of the nitrogen atoms is much closer to three out of four surrounding carbons, thus forming a trigonal pyramidal coordination environment $[C_{3v}]$; Fig. 3(b)], similarly to what was observed in N-doped diamond structures with no clustering defect [56]; the local environment of the second dopant forms an irregular tetrahedron with its neighbors [C_s , Fig. 3(e)]. However, in the N-3-X-C-X system, both nitrogen atoms have the same local $C_{3\nu}$ environment. In the case of a few 16-atom models, the geometry of the cluster defect was such that the effective primitive cell could be built by considering an eight-atom unit; this occurs for the B-, P- and Si-doped structures, which have the symmetries of the orthorhombic space group Amm2 (no. 38), while Al- and N-doped systems require 16-atom supercells with the orthorhombic crystal symmetries of the space group Imm2 (no. 44). The 54-, 128-, and 250-atom systems realize symmetries with either monoclinic Cm (no. 8) or orthorhombic Imm2 (no. 44) symmetry, depending on the local environments of the two dopant atoms, as mentioned at the beginning of the paragraph. In general, structures doped with B, P, and Si are of higher symmetry than those doped with Al and N.

2. Electronic structure analysis

The X-C-X systems doped with Al and B are of p-type with only one energy gap, as is expected in the X-doped cases (see Sec. II in the Supplemental Material [82]). The structures doped with isovalent Si exhibit behavior similar to intrinsic semiconductors with one narrower band gap when compared to the Si-doped X-case; the only exception is the Si-5-X-C-X system realizing two energy gaps, due to the presence of the IB in the middle of the former band gap [Fig. 27(b)]. Moreover, the B-doped structures are forming degenerate p-type semiconductors, as the Fermi level is crossing their valence bands even in the case of the lowest concentration. Systems doped with N in high concentrations (6.25%, 1.85%) exhibit *intrinsiclike* properties; this can be ascribed to the proximity of the defect to its replicas in neighboring cells. Structures doped with N in low concentrations (0.78%, 0.4%) and all of those doped with P form an occupied IB below the CBM, which is typical for *n*-type semiconductors [80]; the position of the P donor band is consistent with other reported investigations [48]. We observe that X-C-X structures doped with N in low concentrations are very similar to X structures, as the impurity level is located at nearly identical depth below the conduction band (Fig. 17). In the case of phosphorus, the X structure is a degenerate *n*-type semiconductor in all concentrations, while X-C-X already forms an intermediate donor band below the CBM at 1.85%. Therefore, in

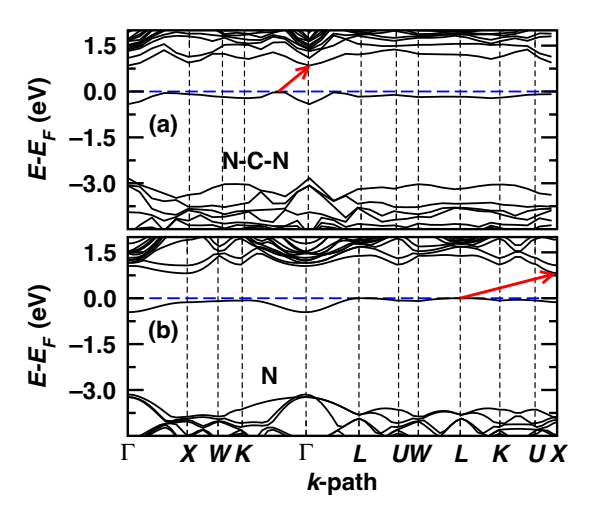


FIG. 17. The electronic band structures of the (a) N-4-X-C-X and (b) N-4-X-V systems. The red arrow connects k-points corresponding to the minimal-energy transition to the conduction band. The Fermi level is set to 0 eV.

the case of P, we can assume that to obtain the impurity level at a certain depth, it is sufficient to use a much lower concentration of X-type defect than of the X-C-X defect.

3. How to engineer the width of the band gap

As mentioned in the previous paragraphs, X-C-X systems contain two main anomalies: (i) N-3-X-C-X has a relaxed geometry that differs from other concentrations, resulting in an insulating structure; and (ii) the size of the band gap of Si-5-X-C-X drops when compared to Si-3-X-C-X and Si-4-X-C-X as a result of a new IB introduced into the energy gap. For this reason, the range of the bandgap sizes can vary as much as more than 2 eV even when we do not consider 6.25% concentration. Without these two anomalies, the band-gap values range within 1.1 eV. This variation is prominent in p-type and Si-doped structures, while the position of the donor level in the *n*-type structures does not change rapidly with the change of concentration. We do not observe any regular trend of the band gap as a function of Hirshfeld charges of the neighbors and the dopant (Fig. 18). However, the change of the Hirshfeld charge with respect to changing concentration is much more significant and irregular when compared to other defect types. Moreover, we observe that dopants with larger atomic radii realize only the positive Hirshfeld charge of the dopant, while the dopants with smaller radii show mostly negative values [Fig. 18(b)]. We do not observe any clear trend of the band gap as a function of the dopant-neighbor bond covalencies $C_{X,C}$ either (Fig. 19). Previously studied X systems [56] have shown a clear $C_{X,C}$ threshold between p- and n-type systems. This threshold is no longer visible due to the significant change of covalency in structures doped with nitrogen; in these cases, the dopant that realizes symmetries of the C_{3v} point

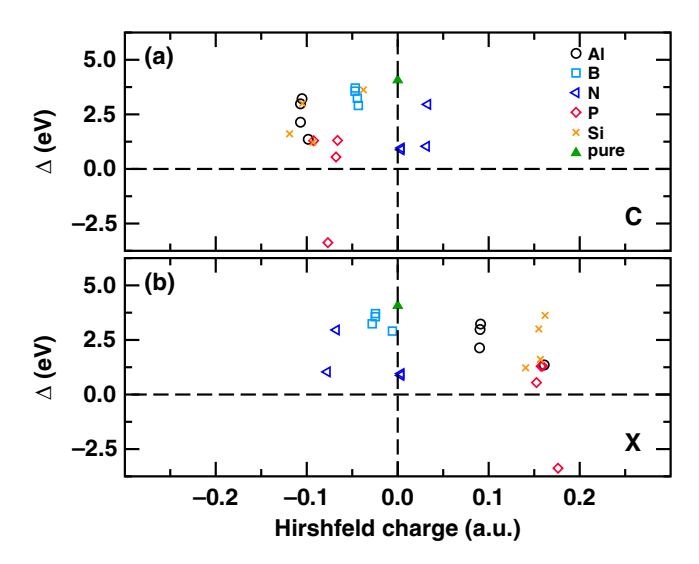


FIG. 18. The generalized band gap as a function of the Hirsh-feld charges of (a) the first neighbors of the dopant and (b) the dopant in the X-C-X systems.

group [Fig. 3(b)] shows high-covalency X—C values, at variance with the reduced covalent character of the bonds of the other dopant. As a result, the average covalency is shifted to considerably lower values when compared to the X case. In fact, the donor band below the CBM is nearly solely formed by states of nitrogen exhibiting high $C_{\rm X}$ C values, without the contribution of the second dopant. If we were to consider the covalency values of this dopant only, at 0.9 eV, we would find the threshold mentioned above as well as a threshold at which the band-gap sizes suddenly decrease. The only exception to this rule is the already mentioned N-3-X-C-X anomaly with a wider band gap. Moreover, it seems that in the majority of the cases, the band gap gets narrower for higher-covalency values at fixed dopant atomic type. This is most notable in the case of silicon, where a sudden rise of covalency in the case of 0.4% concentration correlates with the decrease in the band-gap size.

At first glance, it is apparent that p-type dopants show high positive $\mathcal{P}_{p_x,p_z}(X)$ values while being highly concentration dependent (Fig. 20). At constant concentration, Al-doped systems realize a narrower band gap and higher $\mathcal{P}_{p_x,p_z}(X)$ values compared to B-doped systems. Therefore, we might conclude that a higher $\mathcal{P}_{p_x,p_z}(X)$ means a smaller band-gap size when doped with p-type dopants. On the other hand, systems doped with silicon and ntype systems realize $|\mathcal{P}_{p_x,p_z}(\mathbf{X})| \approx 0$. In fact, the electronic properties of nitrogen-doped systems can be easily distinguished by the $\mathcal{P}_{p_x,p_z}(X)$ values, as negative $|\mathcal{P}_{p_x,p_z}(X)| \approx$ −6% corresponds to the *intrinsiclike* N-2- and N-3-X-C-X structures, while $|\mathcal{P}_{p_x,p_z}(\mathbf{X})| \approx 0$ corresponds to the *n*-type structures of lower concentrations. However, similarly to $C_{X,C}$, the nitrogen-doped *n*-type systems suffer from averaging of the values of the dopants, as the charge of the

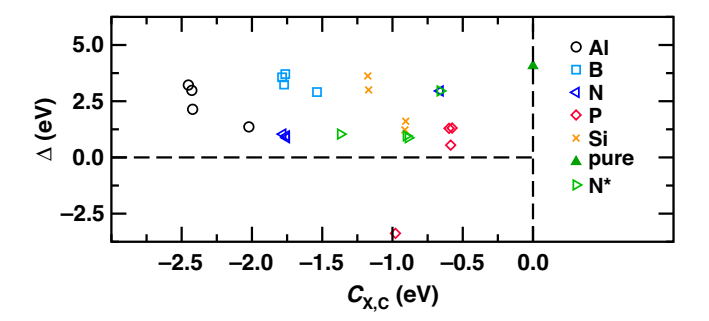


FIG. 19. The generalized band gap as a function of the X—C bond covalency $C_{X,C}$ in X-C-X systems. The N* values correspond to the $C_{X,C}$ of the nitrogen that is responsible for the n-type character of the structure.

first dopant is preferentially distributed along the p_x axis, while it is along the p_z axis for the second dopant; this results in an average $\mathcal{P}_{p_x,p_z}(X)$ value close to zero. We do not find any conclusive results by observing the band-gap size as a function of $\mathcal{P}_{p_x,p_z}(C)$. We observe trends of the $\mathcal{P}_{p_x,p_x}(X,C)$ and $\mathcal{P}_{p_z,p_z}(X,C)$ values that are very similar to those observed in the X cases (Fig. 21). It seems that the decrease of charge at the p-type dopant site ($\mathcal{P}_{p_x,p_x}(X,C)$ and $\mathcal{P}_{p_z,p_z}(X,C)$) of the X—C bond decreases the size of the band gap, while values close to zero and positive values correspond to the n-type dopants. The major deviation from the trend corresponds to the previously mentioned Si-5-X-C-X system.

As we have observed, the systems with higher positive $\mathcal{P}_{p_x,p_z}(X)$ values correspond to the p-type semiconductors, while low absolute $\mathcal{P}_{p_x,p_z}(X)$ values correspond to the n-type semiconductors or silicon-doped structures. The $\mathcal{P}_{p_x,p_x}(X,C)$ and $\mathcal{P}_{p_z,p_z}(X,C)$ values and observed trends

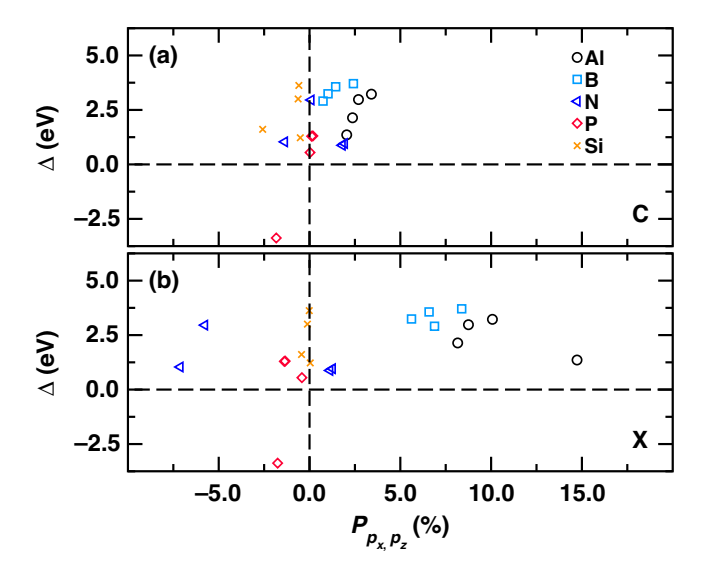


FIG. 20. The generalized band gap as a function of (a) P_{p_x,p_z} (C) and (b) P_{p_x,p_z} (X) in the X-C-X systems.

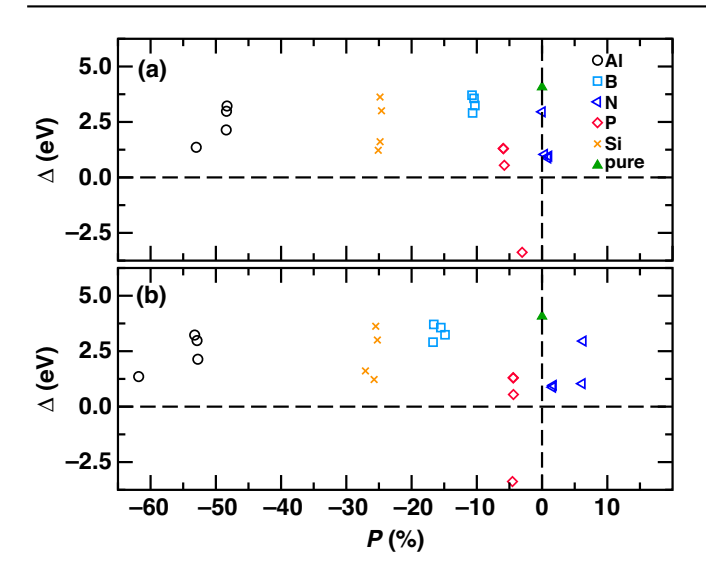


FIG. 21. The generalized band gap as a function of (a) $\mathcal{P}_{p_x,p_x}(X,C)$ and (b) $\mathcal{P}_{p_z,p_z}(X,C)$ in the X-C-X systems.

are very similar to those calculated in the X structures: a decrease of the charge at the dopant side of the X—C bond causes a decrease of the band-gap size. Moreover, the $C_{\rm X,\,C}$ values can still be used to distinguish between p- and n-type structures if we use the $C_{\rm X,\,C}$ of the dopant in the nitrogen-doped systems, which are the major contributor to the band of donor states located below the conduction band, and not the average covalency.

E. X-V-X defect

1. Geometry analysis

In the structures containing X-V-X defects [Fig. 1(d)], each dopant coordinates three carbon atoms. Both dopants have identical or nearly identical local environments. In structures doped with a small-dopant atom (B, N, P), the coordination polyhedra are essentially regular, as only one of the three X—C distances differs by approximately 10^{-2} Å from the other two. On the other hand, similarly to the X-V cases but to a lesser degree, large atoms are situated closer to the former position of the missing carbon; as a result, all three C—X—C bond angles are no longer equivalent. Consequently, one of the X—C distances is noticeably smaller than the other two (realizing point group C_s ; Fig. 3(f) in the case of systems doped with Al or Si (approximately 0.14 and approximately 0.08 Å, respectively). This smaller X—C corresponds to a distance between dopant and carbon that is the most collinear with a dopant-to-dopant line. Similarly to the X-C-X case, when the local geometric environments of the two dopants are the same, the structures possess the symmetries of the orthorhombic Imm2 (no. 44) space group; otherwise, they possess the symmetries of the monoclinic Cm (no. 8) space group; moreover, structures doped with B, P, and Si tend to be of higher symmetry than those doped with Al and N, as for the X-C-X cases.

2. Electronic structure analysis

Unlike in some X-V systems (Al-, P, and Si-doped), a vacancy located between two dopant atoms is maintained after the geometry relaxation of the X-V-X systems. The presence of a vacancy produces the highest amount of localized IBs among the considered systems. Their number increases with decreasing concentration, as a result of the separation of the dopant states from the conduction and valence bands, and ranges between zero and three (B and Si; Fig. 22). This is in good agreement with results documented in the literature (B, Ref. [44]; Si, Ref. [45]). The relative position of the IBs depends on the atomic type of

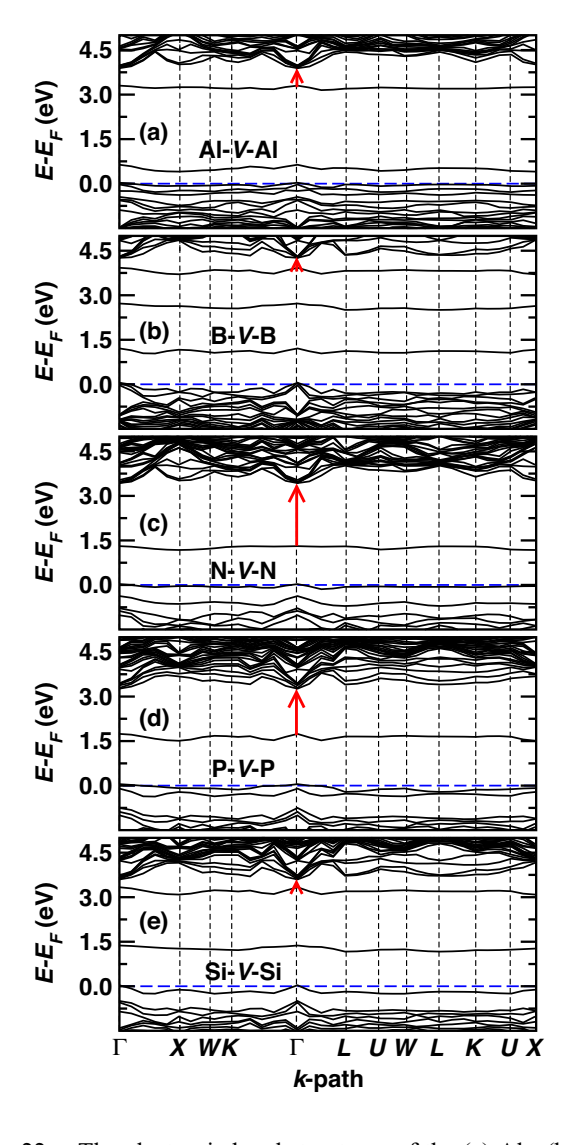


FIG. 22. The electronic band structures of the (a) Al-, (b) B-, (c) N-, (d) P-, and (e) Si-5-X-V-X systems. The red arrow connects k-points corresponding to the minimal-energy transition to the conduction band. The Fermi level is set to 0 eV.

the dopant; however, the majority of the IBs lie above the Fermi level, at variance with the X-V systems, where the Fermi level is found above the majority of IBs. For this reason, the X-V-X systems realize the smallest band gaps of all considered cluster defects, as we often find acceptorlike bands close to the CBM. The band structures of the X-5-X-V-X systems are reported in Fig. 22; we report the lowest considered concentration to show the highest number of IBs and energy gaps.

3. How to engineer the width of the band gap

As we have mentioned previously, the X-V-X systems realize on average the smallest band-gap size when compared to other defects, mostly due to the highest number of IBs added to the energy gap of the pristine structure. Furthermore, all the systems with a non-null band gap show p-type behavior, these being all the systems with a dopant concentration lower than 6.25%. The importance of the effect of changing the dopant concentration on the width of the band gap depends significantly on the band structure of the specific system. This is due to the splitting of the bands from the conduction band, the splitting of IBs, and how we measure the band gap. As an example, we can take a closer look at the boron-doped structures. The largest band gap in boron-doped systems is found at the largest dopant concentration, as all the added states lie at the bottom of the conduction band, this resulting in the single band gap (i.e., no IBs); however, when we slightly decrease the concentration, the bands formed by the dopant split from the conduction band, creating an intermediate small band gap above them (Sec. III A). When we continue to decrease the concentration, the dopant states move deeper toward the valence band, with a corresponding

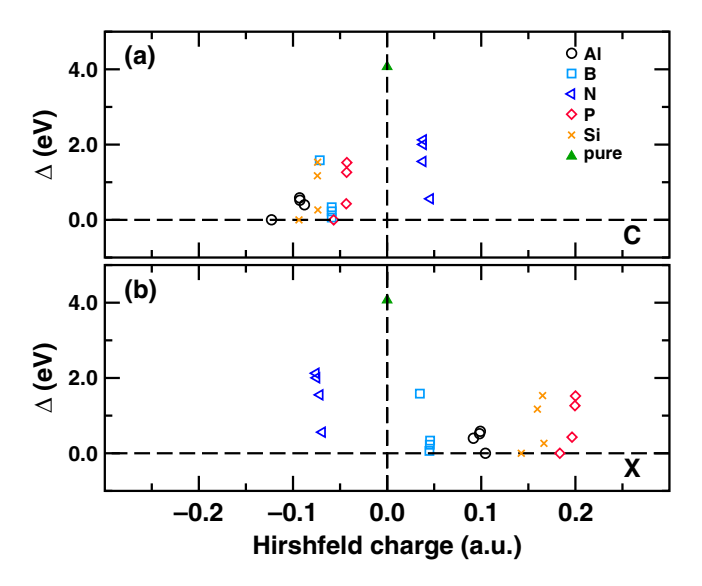


FIG. 23. The generalized band gap as a function of the Hirshfeld charges of (a) the first neighbors of the dopant and (b) the dopant in the X-V-X systems.

expected increase of the band-gap size with the decrease of the dopant concentration. The band-gap size varies by 1.6 eV (1.1 eV between 1.85% and 0.4%) with the concentration but this interval is much lower for the systems that have IBs close to the bottom of the conduction band (Al, B). Hirshfeld-charge analysis does not seem fruitful in finding a general trend even in the case of the X-V-X structures; however, we can observe that the p-type dopants (Al, B) realize the smallest band gap and that their Hirshfeld charges are between 0.04 and 0.11 a.u. Due to this, the resulting plot resembles a parabola [Fig. 23(b)]. We can then conclude that the band-gap size increases with the distance from this interval. Bond covalency seems to be a much better descriptor to tune the band-gap size, as we observe that the band gap reduces drastically when the covalency decreases below -1.5 eV (Fig. 24). We have also found a covalency threshold in the case of the X systems; however, the present case is notably different. In the X systems, the covalency threshold has been a means of distinguishing between p- and n-type structures; in fact, we understand it in such a way that if we increase the bond covalency beyond a certain value, we start to observe the donor states close to the conduction band [56]. On the contrary, in the X-V-X systems, when the covalency decreases below the -1.5 eV threshold, the acceptor states move toward the conduction band, thus reducing the band-gap size. The $C_{X,C}$ values are similar to those of the X systems for the same dopant; thus, n-type dopants still correspond to the highest covalency values. Instead, now the situation is reversed: the p-type dopants form acceptor IBs below the CBM, while the *n*-type dopants form acceptor IBs in the middle of the pristine gap (Fig. 22). In the X-V-X configuration, the dopant neighbors are polarized very slightly [Fig. 25(a)], as the interval of the $\mathcal{P}_{p_x,p_z}(C)$ values around zero has a width of just 3%. We do not see any trend of the band-gap width as a function of $\mathcal{P}_{p_x,p_z}(C)$. However, the $\mathcal{P}_{p_x,p_z}(C)$ values of the structures that do not realize a band gap near the Fermi level are closely packed around -1.35%. By inspecting the dopant polarization $\mathcal{P}_{p_x,p_z}(X)$ [Fig. 25(b)], we observe that the situation is similar to the X-V system. The dopants with large atomic radii (Al, Si,

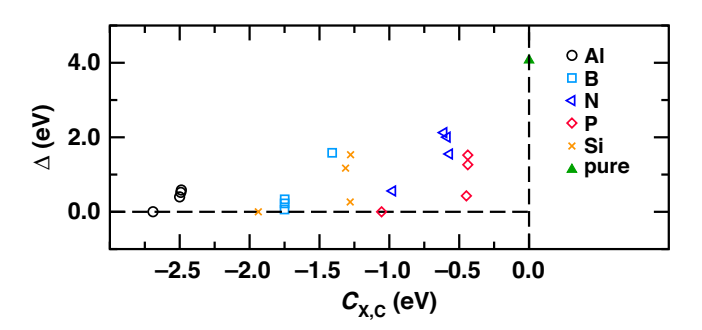


FIG. 24. The generalized band gap as a function of the X—C bond covalency $C_{X,C}$ in the X-V-X systems.

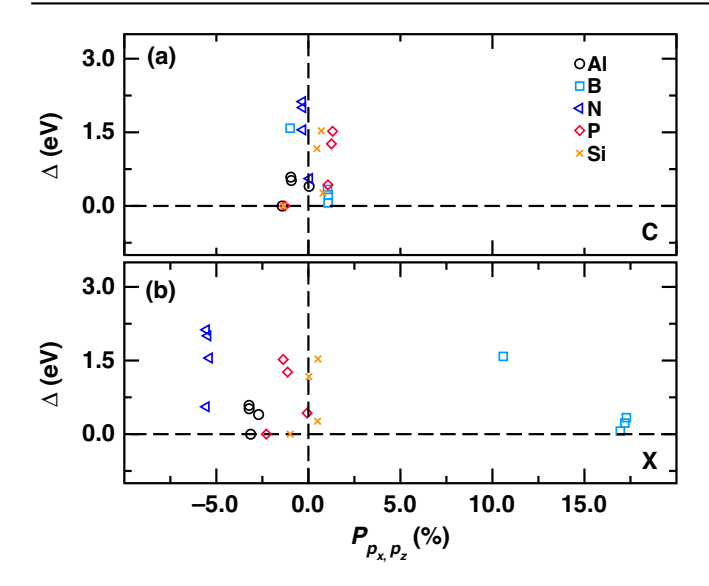


FIG. 25. The generalized band gap as a function of (a) P_{p_x,p_z} (C) and (b) P_{p_x,p_z} (X) in the X-V-X systems.

P) show lower $\mathcal{P}_{p_x,p_z}(X)$ values than small atoms (B, N). However, as the smallest band gaps are realized by the p-type dopants (Al, B) and Si (0.4% concentration) with very different atomic radius, there is no visible trend of the band as a function of $\mathcal{P}_{p_x,p_z}(X)$. We continue by analyzing the $\mathcal{P}_{p_x,p_x}(X, C)$ and $\mathcal{P}_{p_z,p_z}(X, C)$ polarizations (Fig. 26). The observed trends are similar to the other defect types; the values near zero correspond to the n-type dopants. As we have already established, to achieve a lower band gap, we need to choose p-type dopant or Si; as a consequence, a lower $\mathcal{P}_{p_x,p_x}(X, C)$ and $\mathcal{P}_{p_z,p_z}(X, C)$ correspond to the narrowest band gap. We would like to point out

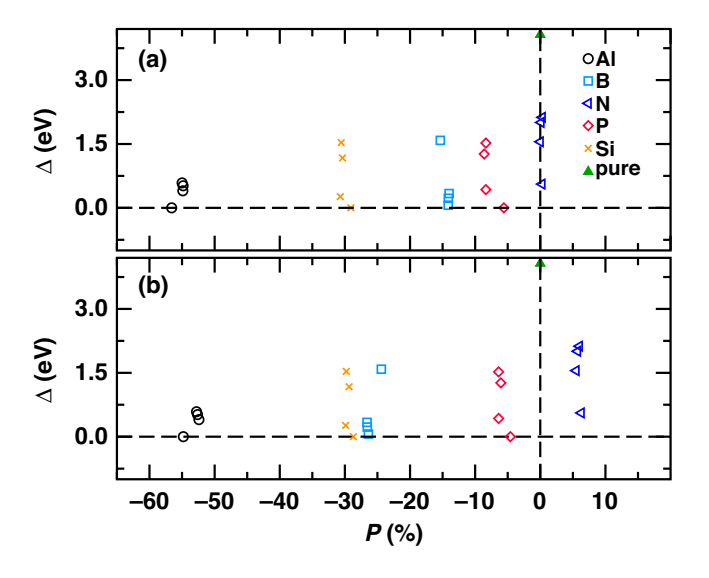


FIG. 26. The generalized band gap as a function of (a) $\mathcal{P}_{p_x,p_x}(X,C)$ and (b) $\mathcal{P}_{p_z,p_z}(X,C)$ in the X-V-X systems.

that Si experiences a drop in band-gap size in the lowest concentration, when one of the bands splits from the conduction band.

We have seen that the size of the band gap does not change monotonically with the change in the concentration of the defect. This is due to the splitting of IBs from the conduction band when the concentration is reduced. We have established that the easiest way to achieve a narrow band gap in X-V-X defects is to choose p-type dopant or Si. This has been manifested by the lowest $C_{X,C}$, $\mathcal{P}_{p_x,p_x}(X,C)$ and $\mathcal{P}_{p_z,p_z}(X,C)$ values.

F. Character of the band gap

In our previous work [56], we have attempted to find a general description that connects the directness of the band gap of the p-type systems to the specific parameter of the system. Our observations have suggested that the directness does not depend on the dopant atomic type but solely on the size of the primitive unit cell. We have seen that in all our systems, the VBM has always been located at Γ , while the position of the CBM has been changing according to the multiplicity of the supercell (i.e., the concentration of the dopant). As we have substituted only a small fraction of the host matrix with the dopant, we have expected band folding to occur. With this assumption, we have calculated where the CBM and VBM k-vectors of the primitive unit cell would be remapped in the supercell. The VBM was always remapped in Γ ; therefore, when the CBM was remapped to (or close to) Γ , we expected a direct band gap. This was indeed consistent with our observation, resulting in 1.85% and 0.4% concentration (corresponding to a multiplicity of 3 and 5 along all three axes) exhibiting a direct band gap.

In the present work, we indeed increase the concentration of the dopants in the equivalent supercell while the concentrations of the cluster defects remain the same. Therefore, we can expect the same rules to be in effect for the cluster defects in a more general manner, as now it is not the concentration of the dopant that dictates the size of the primitive unit cell but the concentration of the cluster defect. However, the situation is now less straightforward, as in many cases we do not observe just one band gap, and the dopant states are not exclusively added only to the top of the valence band or to the bottom of the conduction band. As a consequence, the directness of the measured band gap depends not only on the size of the system but also on which band gap about the Fermi level is selected to measure the directness of the band gap. We observe that systems with the 1.85% and 0.4% concentration of cluster defects possess a direct energy gap between the VBM and the CBM if we define them as follows. As an uppermost band of the valence band, we consider the uppermost band with the negative (concave) curvature at Γ . This band is usually completely or partially

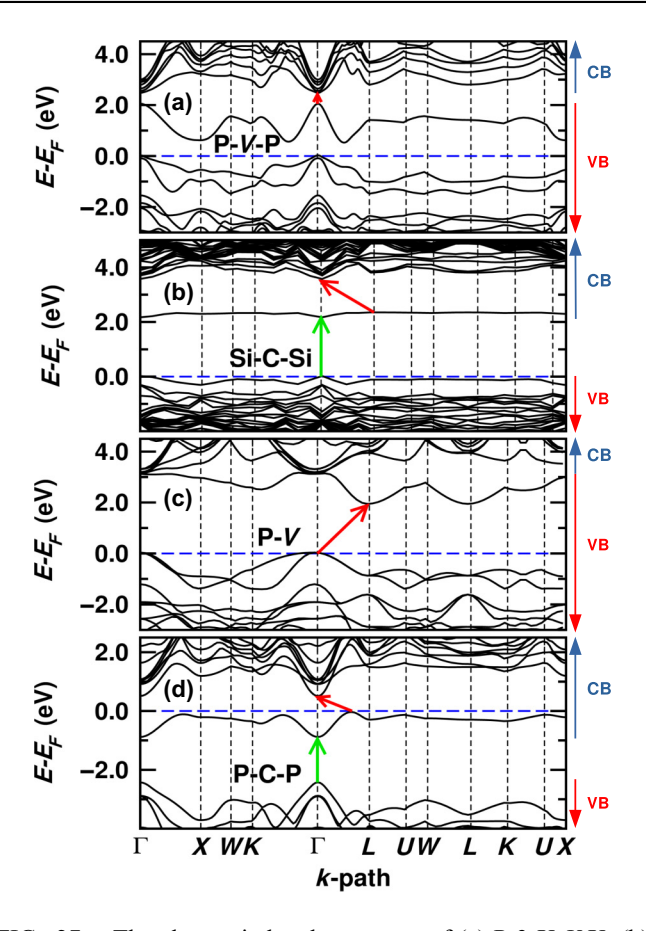


FIG. 27. The electronic band structures of (a) P-3-X-V-X, (b) Si-5-X-C-X, (c) P-3-X-V, and (d) P-3-X-C-X. The red arrow represents the measured band gap according to our definition (Sec. III A), while the green arrow indicates the location of the direct band gap between the top of the valence band and the localized states of the conduction band. The Fermi level is set to 0 eV.

empty and has the behavior of an acceptor band, such as the band below 2 eV in Fig. 27(a). On the other hand, the lowermost band of the conduction band is the lowermost band with positive (convex) curvature. This is commonly a donor band that is fully or partially occupied, as can be seen in Fig. 27(d) right below the Fermi level. Here, we recall that to evaluate the band-gap size, we measure the energy needed to provide the final electron jump to the conductive (delocalized) states in the conduction band. However, this jump can occur between either the localized valence (acceptorlike) or the localized conduction (donorlike) bands and the conductive states of the conduction band. As a consequence, the band gap that we measure is not always the difference between the VBM and the CBM as we have defined them above. Then, three scenarios can occur for p-type structures: (a) a direct energy gap coincides with our definition [Fig. 27(a)]; (b) a localized band representing the conductive state is located below the conduction band, whereas our measured band gap is indirect [Fig. 27(b)]; or (c) the dopant adds valence (acceptor) states that are merged with the conduction band and then the band gap is indirect [Fig. 27(c)]. We note that scenario (a) is the most common in our systems, while (b) and (c) are rare exceptions. The n-type systems are characterized by adding occupied donor states at the bottom of the conduction band; in this case, we will always measure an indirect band gap [Fig. 27(d)]. This is caused by the fact that the donor band as well as the lowermost delocalized band of the conduction band have their minima located at Γ . Therefore, any minimal transition between the top of the donor band and the bottom of the delocalized band has to be indirect.

G. Design rules and technological applications

In this subsection, we focus on selecting the most promising candidate defects and dopants for different technological applications. We summarize the results of the selection in Table III.

1. Degenerate semiconductors

Degenerate semiconductors play a huge role in different fields of modern electronics. One of their most important qualities is that they can be used as transparent conductive materials (TCMs), i.e., materials with sufficiently high electrical conductivity and visible light transparency. The large variety of possible applications of TCMs includes liquid-crystal displays (LCDs), photovoltaics, touch screens, smart windows, and electrodes [94, 95]. Moreover, the extreme properties of diamond (high carrier mobility, hardness, chemical inertness) favor its

TABLE III. A summary of the promising candidates for different technological applications.

Applications	Systems
Transparent conductive materials	All concentrations:
(LCDs, touch screens, electrodes,	B-X, P-X,
lasers, tunnel diodes)	B-X-C-X, P-X-X
	At concentrations $\geq 1.85\%$:
	Al-X-C-X, Al-X,
	Al-X-V-X, $Al-X-V$,
	P-X- <i>V</i> , P-X-C-X,
	Si-X- <i>V</i> -X, B-X-X,
	Si-X-V
IB photovoltaics,	All X-V-X defects,
bioimaging agents	B-X- <i>V</i> , N-X- <i>V</i>
Multicolor emitters	All X-V-X defects,
	B-X- <i>V</i> , N-X- <i>V</i> ,
	N-X-C-X, P-X-C-X,
	N-X-X, V
Optical filters	All defects
•	with a band gap
<i>i</i> -type for PIN diodes	Si-X,
	Si-X-C-X, Si-X-X,
	Al-X-X, N-X-X

use in the above-mentioned applications. Indeed, transparent conductive boron-doped electrodes are already under intensive study and have been experimentally created and tested, especially for use in electrochemistry [96–98]. Current research on TCMs is mainly focused on solving two tasks: the first is to obtain a degenerate *p*-type semiconductor with better conductivity and/or carrier mobility and a sufficiently large band gap (above 3.1 eV for visible light) [99,100], while the second task focuses on designing an ultrawide-band-gap semiconductor transparent for UV light [101]. Beyond the TCMs, degenerate semiconductors are used in tunnel diodes [102] and play a crucial role in achieving population inversion in solid-state lasers (laser diodes) [103] and superluminescent diodes [104].

If we consider potential applications of the material in optoelectronics and TCMs, we are interested in the optical band gap of the material. In degenerate semiconductors, the optical (or apparent) band gap is widened by the width of the occupied (unoccupied) states in the conduction (valence) band of the n-type (p-type) semiconductor. This is called the Moss-Burstein shift [105] and the size of the optical band gap is then equal to the energy required for the smallest possible direct transition between the valence band and an unoccupied state in the conduction band (n-type) or between the occupied states in the valence band and the bottom of the conduction band (p-type). At the largest concentration (6.25%), in some of our systems (B-, P-X-V, Al-, P-, Si-X-V-X), the energy gap near the Fermi level is completely closed by the dopant states; these structures will not be considered in the following discussion, as the energy gap is essential for applications in optoelectronics and TCMs. Nevertheless, they still constitute degenerate semiconductors and can be used as electrodes. We stress that all considered degenerate semiconductors, except for the above-mentioned ones with no gap, have a single energy gap about the Fermi level. IBs in the degenerate semiconductor would indeed increase its optical absorption.

The most effective way to achieve p-type degenerate diamond is to dope it with boron in the X or X-C-X dopant configuration, as the degeneracy is achieved even at the lowest simulated concentrations (0.4%). For the X-C-X systems, this is in agreement with the PDOS analysis, suggesting that the carbon between two dopants plays the major role in causing p-type degeneracy (Sec. III A). The 1.85% concentration seems to be crucial for the nondegenerate-to-degenerate transition, as at this concentration the number of degenerate systems increases significantly (see Fig. 28). Then, as expected, the use of p-type dopant atomic types (Al, B) increases the probability of achieving degeneracy. When the cluster defect consists of a dopant and a vacancy, the situation is more complicated, as the dopant states do not form a compact band but are spread within the band gap. Due to this spread, B-doped structures do not realize p-type degeneracy, while

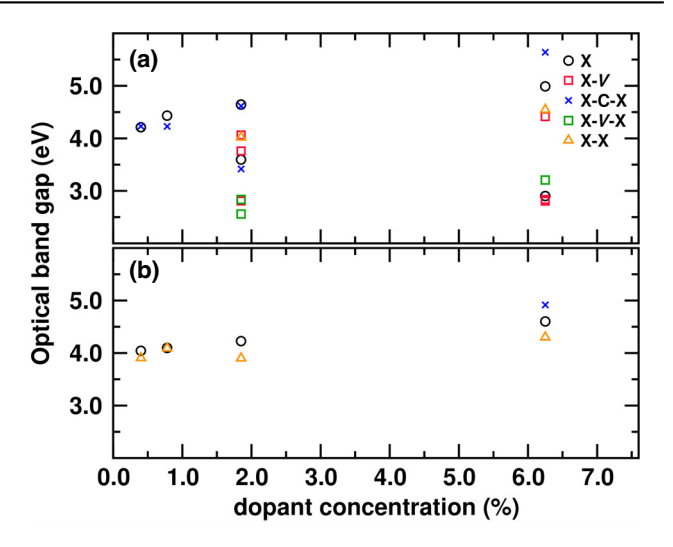


FIG. 28. The optical band gap of the degenerate (a) p-type and (b) n-type diamonds.

systems doped with *n*-type dopants (N, P) or the isovalent Si at larger concentrations do. In the degenerate Al- and Bdoped cases, we observe the highest positive and the most concentration-dependent dopant $\mathcal{P}_{p_x,p_z}(X)$ polarization and the lowest X—C bond covalency $C_{X,C}$. On the other hand, the degenerate *n*-type diamond can be obtained solely by phosphorus doping; this has been obtained in all of the simulated concentrations, when the dopant configuration was X or X-X and once in the X-C-X configuration in the highest concentration. Therefore, it seems that placing any kind of defect other than another phosphorus atom close to the dopant reduces the potential for creating a degenerate ntype diamond. In clear contrast to aluminum and boron, degenerate structures doped with phosphorus are characterized by the lowest $\mathcal{P}_{p_x,p_z}(X)$, $\mathcal{P}_{p_x,p_z}(C)$, $\mathcal{P}_{p_x,p_x}(X,C)$, and $\mathcal{P}_{p_z,p_z}(X, C)$ polarizations and high-covalency $C_{X,C}$ values. Therefore, we may conclude that the extremes of the above-mentioned descriptor values lead to either p-type or n-type degeneracy in certain defect types.

We report the widths of the optical band gap of all degenerate systems in Fig. 28. We observe that an increase in the dopant concentration widens the optical band gap of both p- and n-type systems, with the single exception being the Al-X case. Therefore, the width of the Moss-Burstein shift increases to a greater degree than the size of the energy gap between the valence and conduction band decreases with the increase of the dopant concentrations. p-type systems generally display wider band gaps, especially for boron-doped structures (X, X-C-X) reaching above 5 eV for the highest concentration. The band-gap width of the *n*-type systems reaches above 4.5 eV at the highest concentration, while the systems doped with single phosphorus atom (X) seem to manifest the largest band gaps. The only exception corresponds to the X-C-X system; however, the X-C-X defect forms a degenerate semiconductor only at 6.25% concentration. Such large energies correspond to the UV light up to the UV-C wavelengths and as DFT tends to underestimate the band-gap size, they are probably even larger. However, we may expect a decrease in transparency due to intraband transitions [106]. By analyzing the density of states, we expect that this affects mostly structures with cluster defects at high doping concentrations. The intraband absorption can be reduced by lowering the dopant concentrations due to the fewer electrons (holes) available in the conduction (valence) band; this, however, comes at the cost of reduced conduction. Nevertheless, we expect the majority of the defect-related absorption to be in the infrared wavelengths and the visible or UV transparency to be not affected significantly.

The final selection of the material is therefore a trade-off between conductivity and transparency and depends on the specific application. We may conclude that if transparency is the most important feature for the selected application, then structures doped with boron and phosphorus in the X configuration are the most promising options. On the other hand, if the target application requires high conductivity and lower transparency to visible light is not an issue, cluster defects in high concentrations should be selected. Moreover, even in cases with high conductivity, the UV transparency of the diamond should be preserved [107].

2. Semiconductors with IBs

One of the suggested advanced photovoltaic technologies to overcome the Shockley and Queisser limit of the single-band-gap solar cell [108] is the IB solar cell (IBSC). In the single-band-gap solar cell, the significant part of the spectrum is either not absorbed (energies below the band gap) or is not efficiently utilized due to carrier thermalization (energies above the band gap). Introducing IBs into the band gap by deep-level impurities can increase the absorption of photons with energy lower than the original band gap, as the IBs act as stepping stones on the way to the conduction band. Moreover, high-energy photons are harvested more optimally, as now it is possible to use wideband-gap semiconductors [109-113]. The same principle of photon up-conversion seems promising for the design of the contrast agents, which eliminates the necessity of using UV light in photoluminescence spectroscopy. This would significantly reduce the photodamage and increase the depth of penetration in bioimaging [114,115]. In addition, IB materials can serve as multicolor electroluminescent emitters [116,117]—with suitable control of which interband transition occurs, it might be possible to control the mixing of colors to achieve the desired output color [118]. This, combined with the certain sizes of the energy gaps, would make it possible to create a white light-emitting diode (LED) with simple construction.

We now inspect our systems containing IBs from the point of view of reducing the spectral losses and, thus, increasing the cell efficiency. For simple analysis, we use four parameters: the number, average size, and standard deviation of the energy gaps as well as the average width of the IBs. The standard deviation s_N of the energy-gap sizes is calculated as

$$s_N = \sqrt{\frac{1}{N} \sum_{i=1}^{N} (x_i - \bar{x})^2},$$
 (9)

where the x_i are the sizes and \bar{x} is the arithmetic average of the energy gaps of the studied system, while N is the number of the energy gaps. The standard deviation is a measurement of the dispersion of the considered values; in our case, it conveniently helps us to understand the relative positions of the IBs in the former band gap. Our ultimate goal is to find the most promising candidates for the above-mentioned applications; thus, the most significant parameter is the number of energy gaps, as each added energy gap increases possible options for transition. The second criterion is to find a balance between the average size and standard deviation. A higher standard deviation is preferred to increase the spectral absorption; however, if one of the energy gaps is too large (large average and standard deviation), a significant part of the solar spectrum will not be utilized. Furthermore, IBs with smaller widths are prioritized to decrease the intraband absorption [119]; however, a low number of energy gaps and narrow IBs result in large energy gaps.

By inspecting Fig. 29(a), we immediately note that more than two energy gaps appear only in the X-V systems, while four gaps appear only in systems with X-V-X (B, Si) cluster defects. To achieve three energy gaps with an X-V defect, we need structures in which a vacancy still exists (B, N), i.e., dopant is not forming a regular octahedron with its carbon neighbors. This can be achieved by doping with a dopant with a small atomic radius. As we have discussed in Secs. III A and III E, by decreasing the dopant concentration we split defect bands, thus forming more energy gaps until all bands are split and the number of energy gaps saturates. We proceed by considering the average size and the standard deviation of the energy gaps [Fig. 29(b)]. We observe that X-V structures are again divided into two groups according to their dopant environment. X-V structures doped with large dopants (Al, P, Si) and many X-X (Al, B) and X (Al, N) structures possess a large average band-gap width as well as a large standard deviation; this indicates that the defect state is located close to the conduction or valence band, with one of the energy gaps being significantly larger. We may conclude that these materials will not be suitable for the IBSC, as the larger energy gap tends to be above 3 eV; however, they still might be promising as semiconductor optical-absorption

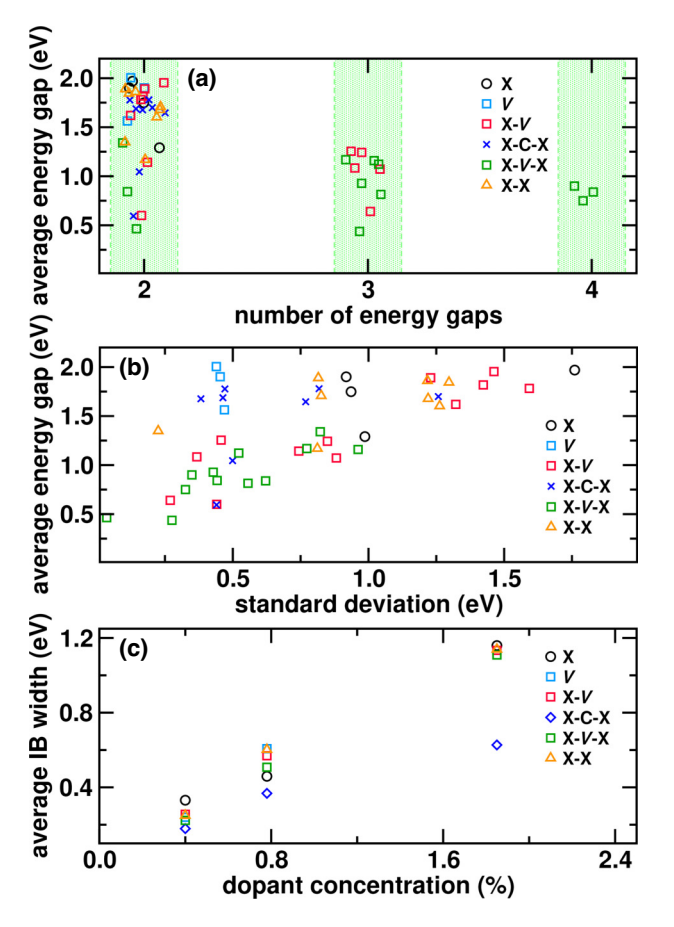


FIG. 29. The average energy gap as a function of (a) the number and (b) the standard deviation of the energy gaps. The values in (a) are intentionally spread around integer numbers corresponding to the number of the energy gap for better readability; the discrete colored regions correspond to different numbers of energy gaps. (c) The average IB width as a function of the dopant concentration.

filters for specific applications, e.g., simultaneous filtering of part of the IR spectrum and all of the UV light [120]. The materials with a vacancy (V) or an X-C-X defect (N, P) and X-X (N) show large average energy-gap widths and low standard deviation values while realizing only two energy gaps. This means that the bands formed by the defect states are located near the middle of the band gap; such systems achieve higher absorption efficiencies than the above-mentioned systems, especially when doped in high concentrations to decrease the sizes of the gaps. However, due to the two large energy gaps with the sizes corresponding to the energies of the visible light, these structures have a greater potential of being used as multicolor emitters rather than as IBSCs. The last group of systems possesses average energy-gap values around 1 eV and lower standard deviations. These are mostly systems containing a vacancy and a dopant: X-V doped with dopants with small atomic radii (B, N) and X-V-X structures. The X-V structures (B, N) and X-V-X structures doped with Al and N still contain one relatively large gap (>1.5 eV) when doped in lower concentrations; nonetheless, three energy gaps provide many options for possible transitions. The remaining structures (B-, P-, Si-X-V-X) represent the most promising candidates for IBSC materials, as they possess the largest number of energy gaps, at least one of the energy gaps being under 0.5 eV, while there is no larger energy gap than 1.5 eV; therefore, the solar spectrum can be utilized in the most efficient manner. The last considered parameter, the average IB width for each defect type and three lower concentrations, is reported in Fig. 29(c). As expected, with lowering concentration, the bands become more localized, which corresponds to a decrease of the IB width. We recall that wide IBs decrease the efficiency because of the intraband transitions; to avoid this effect, it is more efficient to choose a low concentration of the dopant.

In this subsection, we have analyzed IB materials to estimate their potential for maximizing solar-spectral absorption. We have observed that the promising candidates for IBSCs are the structures doped with cluster defects consisting of both dopant(s) and a vacancy, while X-V-X systems doped with B, P and Si seem to utilize the solar spectrum most efficiently. The increase of defect concentration can help in decreasing the sizes of the energy gaps of the X-V (B, N), X-C-X (N, P), X-X (N), and V systems, at the cost of the increase of the width of the IBs. The IB structures with a very wide energy gap are the least suitable for photon up-conversion applications: this includes systems doped with X (Al, N), X-V (Al, P, Si) and X-X (Al, B). Nevertheless, all IB structures might be useful for specific applications such as multicolor emitters or optical filters, where emitting or blocking certain wavelengths is desired.

3. Semiconductor type and activation energies

In this subsection, we will analyze which of the studied systems are *p*-type, *n*-type, or if they show *intrinsiclike* (or i-type) behavior; then, we will qualitatively examine the effect of the different dopants and cluster defects on the activation energy. In the following discussion, we focus on the lower concentrations of the defect, where the observed features (e.g., positions of the impurity bands) do not change so rapidly with the change of the concentration. Therefore, we do not expect these trends to change even at lower concentrations than simulated. We acknowledge that the number of carriers in structures with deep impurities would be very low under standard conditions; however, the defect can still be classified as p-type or n-type even with low conductivity of the material. We are also aware that this description is based on the assumption that a defect classification as p-type or n-type translates directly into the material conductivity type. However, in real materials, the presence of different impurities and external stimuli can lead to charge-compensation effects, where the formation of charged defects may reduce the number of free carriers and alter the expected electrical behavior (see Sec. II). Therefore, even if the defect is nominally *p*-type or *n*-type, the overall electrical behavior of the material may differ from this idealized classification. A more rigorous analysis of how defects influence conductivity would require the calculation of ionization energies to determine the stability of different charge states at various Fermi levels [75]. Our distinction between types is based on the band structure and the position of the Fermi level in the following way [80]:

- (1) *p-type*. The band structure is characterized by a completely or partially empty impurity band located in the band gap or merged with the valence band; if the impurity band is only partially empty, then it is closer to the valence than to the conduction band, i.e., it is energetically more favorable to promote an electron from the valence band to the impurity band than to promote an electron from the impurity band to the conduction band. Moreover, the shape of the impurity band can indicate if it originates from the valence or the conduction band [negative curvature at Γ ; see Fig. 27(a)].
- (2) *n-type*. The band structure is characterized by a completely or partially full impurity band located in the band gap or merged with the conduction band; if the impurity band is only partially full, then it is closer to the conduction than to the valence band, i.e., it is energetically more favorable to promote an electron from the impurity band to the conduction band than to promote an electron from the valence band to the impurity band. Moreover, the shape of the impurity band can indicate if it originates from the valence or the conduction band [positive curvature at Γ ; see Fig. 27(d)].
- (3) *i-type*. The band structure is characterized by a large energy gap between the fully occupied impurity band located close to the valence band and the nearest unoccupied band in the conduction band [see Figs. 7(a)–7(b)]. These systems behave as *intrinsic* semiconductors.

As mentioned in the previous subsections, *p*-type dopants (Al, B) usually form *p*-type semiconductors while *n*-type dopants (N, P) usually form *n*-type semiconductors, as expected. However, there are a few exceptions to this rule. The *n*-type dopants can form *p*-type structures if a vacancy is part of the cluster defect. Moreover, both *p*- and *n*-type dopants can form structures that show behavior characteristic of *intrinsic* (i.e., *i*-type) semiconductors; this has been observed in the X-X systems, where two neighboring Al atoms and two neighboring N atoms seem to compensate for each other. In the majority of the cases, the isovalent dopant Si forms *i*-type structures, with the exception of the systems containing a vacancy (X-V and X-V-X) and systems that are *p*-type semiconductors. The *i*-type systems are promising candidates for codoping, as the introduction

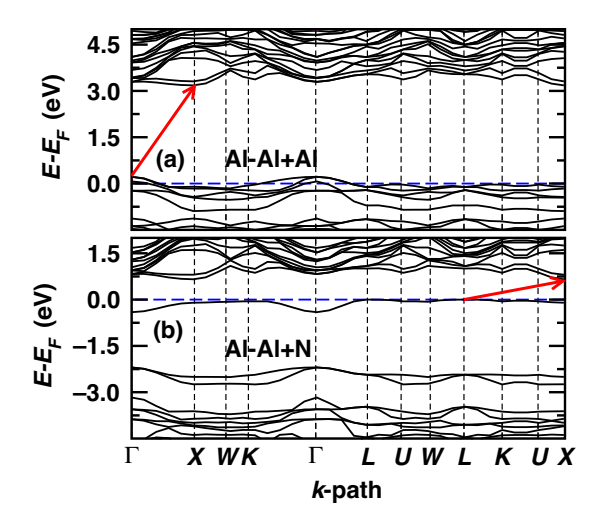


FIG. 30. The electronic band structures of the Al-4-X-X structure additionally doped with (a) Al and (b) N. The red arrow connects k-points corresponding to the minimal-energy transition to the conduction band. The Fermi level is set to 0 eV.

of another impurity to the structure (e.g., Al or N) can determine if the structure will be *p*-type or *n*-type. Furthermore, the introduction of different types of impurities can tune the edges of the valence and conduction bands, and thus the band gap, as well as increasing the number of IBs in the former band gap [121]. As an example, we have indeed doped a few insulating structures with single Al and N dopants located equidistantly between the original defects, i.e., as far from them as possible. By calculating the optimized geometry and the band structures, we have proved the above-mentioned assumptions and two of the band structures are reported in Fig. 30. We report all the studied systems divided into categories based on their type of conductivity in Table IV.

Another extremely important quantity for technological applications is the activation energy of the dopant. The activation energy indicates the amount of free carriers, and thus the conductivity, at a given temperature. Therefore, for the majority of the applications, it is necessary to dope the semiconductor with defects with sufficiently low activation energies to obtain adequate conductivity at room temperature [75,122]. The task of obtaining shallow defect levels corresponding to low activation energies in the case of the wide-band-gap semiconductors is especially difficult [121]. The p-type diamond has been successfully created with relatively low activation energies with boron doping [123], while achieving useful *n*-type doping is still a significant challenge [124]. Doping with phosphorus seems to be the most promising single-donor dopant; however, high dopant concentrations are required to obtain shallow impurity levels [19]. This problem has been tackled by many ab initio studies focused on codoping [77,125-127]. To this aim, we attempt to order different types of defects based on their activation energies irrespective of

TABLE IV. The division of the systems into categories based on the type of conductivity.

X	p-type	<i>n</i> -type	i-type
Al	X, X-V		X-X
	X-C-X		
	X-V-X		
В	X, X-V		
	X-C-X		
	X-V-X, X-X		
N	X-V	X	X-X
	X-V-X	X-C-X	
P	X-V	X, X-C-X	
	X-V-X	X-X	
Si	X-V		X, X-C-X
	X-V-X		X-X
V	X		

the concentration; we recall that all the assumptions in this subsection are meant for low concentrations. Our qualitative analysis is mostly based on the depth of the dopant states in the band gap. In a few cases, we observe inconclusive results, e.g., two types of defects form a degenerate semiconductor even at the lowest concentration. We then decide by analyzing the density of states; we inspect which system has an impurity band that has a higher chance of detaching from the valence (conduction) band when the concentration is further reduced. As an example, we proceed as follows. We observe that the B-X defect forms a degenerate semiconductor, while the B-X-X defect forms a band of acceptor states 0.7 eV above the valence band at the same concentration; therefore, we conclude that the B-X defect has a lower activation energy than the B-X-X defect. The exact activation energies would require significantly more intensive calculations, such as considering structures with charged defects and their formation energies [75], which is beyond the scope of this work. Our findings are reported in Table V from the largest to the smallest (left to right) activation energy for each dopant atom. We mark systems with the "(p)," "(n)," and "(i)" labels corresponding to the type of the system (p-, n-, or itype), wherever it helps to highlight the contrast with other systems in the same row. The systems doped with N and P are both split into two rows to compare activation energies for p- and n-type systems separately.

We observe that only a few defect-cluster types can decrease the activation energy when compared to the single-dopant case. The most prominent example is the X-C-X system, which decreases the activation energy for both *p*-type dopants and nitrogen-doped structures. However, in the case of N-X-C-X, the improvement is so small that both activation energies can be said to be equivalent; moreover, we do not see any improvement in the case of a phosphorus-doped structure, which is far more interesting due to the shallower donor levels. On the other

TABLE V. The ordering of the systems according to their activation energy, from the highest to the lowest (left to right), for each dopant atom. The "(p)," "(n)," and "(i)" labels correspond to the type of the system (p-, n-, or i-type) and are added wherever they help to highlight the contrast with other systems in the same row. The systems doped with N and P are both split into two rows to compare activation energies for p- and n-type systems separately.

X	Activation energy (>)					
Al	X-X(i)	X-V-X	X-V	X	X-C-X	
В	X-V	X-V-X	X-X	X	X-C-X	
N(p)	X-V-X			X-V		
N(n)	X-X(i) X			X-C-X		
P(p)	X-V-X			X-V		
P(n)	X-C-X X-X		X			
Si	X	X-C-X	X-X	X-V-X(p)	X-V(p)	

hand, the use of the X-X defects increases the depth of the impurity bands in all cases—which, in all cases except for the isovalent silicon, leads to the increase of the activation energy.

IV. CONCLUSIONS

In this work, we have attempted to uncover coupled structural-electronic features of different cluster defects formed by aggregation of dopant and/or vacancies. To this aim, we have conducted a quantum mechanical investigation of four different defect types: (a) dopant-vacancy complexes (X-V), (b) two dopants as nearest neighbors (X-X), (c) two dopants separated by one carbon atom (X-C-X), and (d) two dopants separated by a vacancy (X-V-X). For each of these structures, we have considered Al, B, N, P, and Si as dopant atoms. The cluster defects have been compared with the single-dopant case (X) wherever relevant.

We have seen that the dopant atomic radius plays a crucial role in determining the local environment of the dopant in the X-V complexes. The large-dopant atoms (Al, P, Si) form octahedrons with their neighbors, while the small dopants (B, N) form trigonal pyramidal configurations. In the case of other cluster defects, we have very rarely found the change of point group characterizing the local environment of the dopant with the change of the concentration or the dopant atomic type. We have seen that the number and positions of the IBs added to the former band gap of pristine diamond depends on the dopant atomic type as well as on the cluster-defect type. The X-V doped with large atoms, X-X, and X-C-X structures, always add a single IB, while X-V doped with small atoms and an X-V-X defect add up to three IBs.

We have found that irrespective of the type of defect, the n-type dopants realize the most covalent bonds of all studied dopants. This is true even in the case of structures containing a vacancy, which show p-type behavior even

when doped with *n*-type dopant. To achieve the smallest band gap with the X-V cluster, we need to choose smalldopant atoms; such atoms cause significant dominance of charge at the dopant site along one of the axes with respect to the other. When a small-dopant atom is selected, we can decrease the band-gap size even further by choosing a dopant that is an electron acceptor. Moreover, by comparing all structures containing a single p-type dopant atom, we have been able to order the band-gap sizes with respect to the coordination number (CN) of the dopant from widest to narrowest as follows: tetrahedral (CN = 4), octahedral (CN = 8), and trigonal pyramidal (CN = 3) dopant coordination. The X-X structures often form more insulating structures than other defect types. This is caused by the self-compensation of the two dopants of the same atomic type and is most apparent for Al and N, which exhibit behavior similar to the intrinsic semiconductors. On the other hand, P-doped structures constitute the degenerate semiconductor similarly to the X case. In X-X structures, the covalency, and the orbital polarizations of the dopant and their neighboring carbons, seemed to be the promising parameters to engineer the desired band-gap size. The positive band gap can be narrowed by the increase of the covalency as well as by the increase of the polarization of the dopant and neighboring carbons. The p-type dopants in the X-C-X arrangement act in a very similar way to their counterparts in the X configuration. The best descriptor to tune the band-gap size in these systems is by charge redistribution along the X—C bond axis. We have found that the increase of the charge at the dopant side of the bond increases the size of the band gap. We have observed that the band-gap width of X-V-X systems does not change monotonically with the change of concentration. This is a consequence of the splitting of the intermediate impurity bands from the conduction band. In these systems, the band-gap size mostly depends on whether the dopant is of p-type or n-type. The smallest band gaps are realized by p-type dopants and Si, which realize the most ionic bonds. How to achieve the directness of the band gap in diamond-based materials has been extensively discussed in our previous work on structures doped with single-dopant atoms. In this work, we have found that the directness of the band gap depends solely on the multiplicity of the supercell (i.e., the doping concentration) even in the case of cluster defects. However, due to the presence of multiple energy gaps about the Fermi level, this direct band gap is not always the band gap that we have measured for our analysis.

In the last part of our work, we have focused on technological applications of the cluster defects. We have evaluated that the most promising dopants for transparent conductive materials are B (*p*-type) and P (*n*-type) in the X configuration and that they realize optical band gaps corresponding to the UV-C wavelengths. If transparency is not a requirement, P-X-X (*n*-type) and B-X-C-X (*p*-type)

defects can be used to increase the conductivity. By analyzing the structures with IBs, we have concluded that X-V-X systems doped with Si and B utilize the solar spectrum to the greatest extent. This is due to their having the largest number of IBs and to their optimal spacing in the band gap of the pristine diamond, which maximizes the optical absorption. Other IB structures may find their application in multicolor emitters and optical filters, among others. Lastly, we have analyzed the depth of the impurity levels to determine the dopant activation energies. Unfortunately, we have not found any defect configuration that will realize a much-needed decrease in the activation energy of *n*-type phosphorus when compared to its X configuration. In fact, the cluster defects seem to increase the activation energy with respect to the X case in the majority of cases. The only exceptions are X-C-X (Al, B, N), and all cluster defects of isovalent Si.

This work represents a set of suggestions on how to choose optimal dopant atomic types, their concentrations, and their aggregation to achieve the desired electronic or optical properties. The final subsections are dedicated to several technological applications well suited for cluster defects. The reader is already presented with a variety of promising options for specific applications, which can be promptly used in the design of particular devices.

ACKNOWLEDGMENTS

This work was supported by the project "The Energy Conversion and Storage," funded as Project No. CZ.02.01.01/00/22_008/0004617 by Programme Johannes Amos Commenius, of the Excellent Research call. This work was supported by the Ministry of Education, Youth, and Sports of the Czech Republic through the e-INFRA CZ (ID:90254). The access to the computational infrastructure of the OP-VVV—funded Project No. CZ.02.1.01/0.0/0.0/16_019/0000765, "Research Center for Informatics," is also gratefully acknowledged.

All authors have contributed equally.

The authors declare that they have no known competing financial interests or personal relationships that could have appeared to influence the work reported in this paper.

^[1] C. J. Wort and R. S. Balmer, Diamond as an electronic material, Mater. Today 11, 22 (2008).

^[2] J. Isberg, J. Hammersberg, D. Twitchen, and A. White-head, Single crystal diamond for electronic applications, Diam. Relat. Mater. 13, 320 (2004). carbon Materials for Active Electronics. Proceedings of Symposium L, E-MRS Spring Meeting 2003.

^[3] G. Perez, A. Maréchal, G. Chicot, P. Lefranc, P.-O. Jeannin, D. Eon, and N. Rouger, Diamond semiconductor

- performances in power electronics applications, Diam. Relat. Mater. 110, 108154 (2020).
- [4] M. Panizza and G. Cerisola, Application of diamond electrodes to electrochemical processes, Electrochim. Acta 51, 191 (2005).
- [5] T. Shimaoka, S. Koizumi, and M. M. Tanaka, Diamond photovoltaic radiation sensor using *pn* junction, Appl. Phys. Lett. 113, 093504 (2018).
- [6] A. Aleksov, M. Kubovic, N. Kaeb, U. Spitzberg, A. Bergmaier, G. Dollinger, T. Bauer, M. Schreck, B. Stritzker, and E. Kohn, Diamond field effect transistors—concepts and challenges, Diam. Relat. Mater. 12, 391 (2003). 13th European Conference on Diamond, Diamond-Like Materials, Carbon Nanotubes, Nitrides and Silicon Carbide.
- [7] H. Kato, T. Makino, M. Ogura, D. Takeuchi, and S. Yamasaki, Fabrication of bipolar junction transistor on (001)-oriented diamond by utilizing phosphorus-doped *n*-type diamond base, Diam. Relat. Mater. **34**, 41 (2013).
- [8] Y. Gurbuz, O. Esame, I. Tekin, W. P. Kang, and J. L. Davidson, Diamond semiconductor technology for rf device applications, Solid State Electron. 49, 1055 (2005).
- [9] D. Eon, A. Traoré, J. Pernot, and E. Gheeraert, in 2016 28th International Symposium on Power Semiconductor Devices and ICs (ISPSD) (IEEE, 2016), pp. 55–58, https://ieeexplore.ieee.org/document/7520776.
- [10] V. Jha, H. Surdi, M. Faizan Ahmad, F. Koeck, R. J. Nemanich, S. Goodnick, and T. J. Thornton, Diamond Schottky p-i-n diodes for high power rf receiver protectors, Solid State Electron. 186, 108154 (2021).
- [11] M. Suzuki, T. Sakai, T. Makino, H. Kato, D. Takeuchi, M. Ogura, H. Okushi, and S. Yamasaki, Electrical characterization of diamond PiN diodes for high voltage applications, Phys. Status Solidi (a) 210, 2035 (2013).
- [12] W. Huang, T. P. Chow, J. Yang, and J. E. Butler, High-voltage diamond Schottky rectifiers, Int. J. High Speed Electron. Syst. 14, 872 (2004).
- [13] M. A. Prelas, in Laser Interaction and Related Plasma Phenomena: Volume10, edited by G. H. Miley and H. Hora (Springer US, Boston, Massachusetts, 1992), pp. 403–419.
- [14] T. Braun, S. Kucheyev, S. Shin, Y. Wang, J. Ye, N. Teslich, C. Saw, D. Bober, E. Sedillo, N. Rice, K. Sequoia, H. Huang, W. Requieron, A. Nikroo, D. Ho, S. Haan, A. Hamza, C. Wild, and J. Biener, Tungsten doped diamond shells for record neutron yield inertial confinement fusion experiments at the national Ignition Facility, Nucl. Fusion 63, 016022 (2022).
- [15] P. Calvani, A. Bellucci, M. Girolami, S. Orlando, V. Valentini, R. Polini, and D. M. Trucchi, Black diamond for solar energy conversion, Carbon 105, 401 (2016).
- [16] J. Raymakers, A. Artemenko, S. S. Nicley, P. Štenclová, A. Kromka, K. Haenen, W. Maes, and B. Rezek, Expanding the scope of diamond surface chemistry: Stille and Sonogashira cross-coupling reactions, J. Phys. Chem. C 121, 23446 (2017).
- [17] M. Mori, Y. Saeki, M. Hakamata, T. Sato, E. Kabasawa, and J. Nakamura, Electronic structures of aluminum-doped diamond near the Fermi level, J. Phys. Soc. Jpn. 84, 044704 (2015).

- [18] S. Heyer, W. Janssen, S. Turner, Y.-G. Lu, W. S. Yeap, J. Verbeeck, K. Haenen, and A. Krueger, Toward deep blue nano Hope diamonds: Heavily boron-doped diamond nanoparticles, ACS Nano 8, 5757 (2014).
- [19] T. Grotjohn, D. Tran, M. Yaran, S. Demlow, and T. Schuelke, Heavy phosphorus doping by epitaxial growth on the (111) diamond surface, Diam. Relat. Mater. 44, 129 (2014).
- [20] Y. N. Palyanov, I. N. Kupriyanov, Y. M. Borzdov, A. F. Khokhryakov, and N. V. Surovtsev, High-pressure synthesis and characterization of Ge-doped single crystal diamond, Cryst. Growth Des. 16, 3510 (2016).
- [21] B. Yang, J. Li, L. Guo, N. Huang, L. Liu, Z. Zhai, W. Long, and X. Jiang, Fabrication of silicon-vacancy color centers in diamond films: Tetramethylsilane as a new dopant source, CrystEngComm 20, 1158 (2018).
- [22] M. Kasu and M. Kubovic, Arsenic-doped n-type diamond grown by microwave-assisted plasma chemical vapor deposition, Jpn. J. Appl. Phys. 49, 110209 (2010).
- [23] E. Rohrer, C. F. O. Graeff, R. Janssen, C. E. Nebel, M. Stutzmann, H. Güttler, and R. Zachai, Nitrogen-related dopant and defect states in CVD diamond, Phys. Rev. B 54, 7874 (1996).
- [24] I. Sakaguchi, M. N.-Gamo, Y. Kikuchi, E. Yasu, H. Haneda, T. Suzuki, and T. Ando, Sulfur: A donor dopant for *n*-type diamond semiconductors, Phys. Rev. B **60**, R2139 (1999).
- [25] M. Biener, J. Biener, S. Kucheyev, Y. Wang, B. El-Dasher, N. Teslich, A. Hamza, H. Obloh, W. Mueller-Sebert, M. Wolfer, T. Fuchs, M. Grimm, A. Kriele, and C. Wild, Controlled incorporation of mid-to-high Z transition metals in CVD diamond, Diam. Relat. Mater. 19, 643 (2010). proceedings of Diamond 2009, The 20th European Conference on Diamond, Diamond-Like Materials, Carbon Nanotubes and Nitrides, Part 1.
- [26] H. Sumikura, K. Hirama, K. Nishiguchi, A. Shinya, and M. Notomi, Highly nitrogen-vacancy doped diamond nanostructures fabricated by ion implantation and optimum annealing, APL Mater. 8, 031113 (2020).
- [27] L. Childress and R. Hanson, Diamond NV centers for quantum computing and quantum networks, MRS Bull. 38, 134 (2013).
- [28] I. Aharonovich, S. Castelletto, D. A. Simpson, C.-H. Su, A. D. Greentree, and S. Prawer, Diamond-based singlephoton emitters, Rep. Prog. Phys. 74, 076501 (2011).
- [29] J. L. Webb, J. D. Clement, L. Troise, S. Ahmadi, G. J. Johansen, A. Huck, and U. L. Andersen, Nanotesla sensitivity magnetic field sensing using a compact diamond nitrogen-vacancy magnetometer, Appl. Phys. Lett. 114, 231103 (2019).
- [30] C. Bradac, W. Gao, J. Forneris, M. E. Trusheim, and I. Aharonovich, Quantum nanophotonics with group IV defects in diamond, Nat. Commun. 10, 5625 (2019).
- [31] J. R. Maze, P. L. Stanwix, J. S. Hodges, S. Hong, J. M. Taylor, P. Cappellaro, L. Jiang, M. V. G. Dutt, E. Togan, A. S. Zibrov, A. Yacoby, R. L. Walsworth, and M. D. Lukin, Nanoscale magnetic sensing with an individual electronic spin in diamond, Nature 455, 644 (2008).
- [32] I. Aharonovich and E. Neu, Diamond nanophotonics, Adv. Opt. Mater. 2, 911 (2014).

- [33] S. Castelletto, L. Rosa, J. Blackledge, M. Z. Al Abri, and A. Boretti, Advances in diamond nanofabrication for ultrasensitive devices, Microsyst. Nanoeng. 3, 17061 (2017).
- [34] S. Schietinger, M. Barth, T. Aichele, and O. Benson, Plasmon-enhanced single photon emission from a nanoassembled metal-diamond hybrid structure at room temperature, Nano Lett. 9, 1694 (2009).
- [35] E. Ekimov and M. Kondrin, Vacancy-impurity centers in diamond: Perspectives of synthesis and applications, Uspekhi Fizicheskih Nauk 60, 539 (2016).
- [36] M. Capelli, A. Heffernan, T. Ohshima, H. Abe, J. Jeske, A. Hope, A. Greentree, P. Reineck, and B. Gibson, Increased nitrogen-vacancy centre creation yield in diamond through electron beam irradiation at high temperature, Carbon 143, 714 (2019).
- [37] J. O. Orwa, I. Aharonovich, F. Jelezko, G. Balasubramanian, P. Balog, M. Markham, D. J. Twitchen, A. D. Greentree, and S. Prawer, Nickel related optical centres in diamond created by ion implantation, J. Appl. Phys. 107, 093512 (2010).
- [38] J. P. Goss, R. J. Eyre, and P. R. Briddon, Theoretical models for doping diamond for semiconductor applications, Phys. Status Solidi (b) **245**, 1679 (2008).
- [39] J. Walker, Optical absorption and luminescence in diamond, Rep. Prog. Phys. 42, 1605 (1979).
- [40] M. N. R. Ashfold, J. P. Goss, B. L. Green, P. W. May, M. E. Newton, and C. V. Peaker, Nitrogen in diamond, Chem. Rev. 120, 5745 (2020).
- [41] V. Nadolinny, Y. N. Palyanov, Y. M. Borzdov, M. Rakhmanova, A. Y. Komarovskikh, and O. Yurjeva, HTHP treatment of diamonds containing N1 centers. Neutral state of the N1 center as a limiting step in the aggregation of substitutional nitrogen into a form, Diam. Relat. Mater. 141, 110632 (2024).
- [42] P. Ashcheulov, J. Šebera, A. Kovalenko, V. Petrák, F. Fendrych, M. Nesládek, A. Taylor, Z. Vlčková Živcová, O. Frank, L. Kavan, M. Dračínský, P. Hubík, J. Vacík, I. Kraus, and I. Kratochvílová, Conductivity of boron-doped polycrystalline diamond films: Influence of specific boron defects, Eur. Phys. J. B 86, 443 (2013).
- [43] V. Nadolinny, A. Komarovskikh, Y. Palyanov, and A. Sokol, EPR of synthetic diamond heavily doped with phosphorus, Phys. Status Solidi (a) **212**, 2568 (2015).
- [44] J. P. Goss and P. R. Briddon, Theory of boron aggregates in diamond: First-principles calculations, Phys. Rev. B 73, 085204 (2006).
- [45] J. P. Goss, P. R. Briddon, and M. J. Shaw, Density functional simulations of silicon-containing point defects in diamond, Phys. Rev. B **76**, 075204 (2007).
- [46] K. Iakoubovskii and G. Adriaenssens, Optical detection of defect centers in CVD diamond, Diam. Relat. Mater. 9, 1349 (2000).
- [47] T. Miyazaki and S. Yamasaki, Ab initio energetics of phosphorus related complex defects in synthetic diamond, Physica B 376–377, 304 (2006). proceedings of the 23rd International Conference on Defects in Semiconductors.

- [48] J. P. Goss, R. J. Eyre, and P. R. Briddon, Bound substitutional impurity pairs in diamond: A density functional study, J. Phys.: Condens. Matter **20**, 085217 (2008).
- [49] R. J. Eyre, J. P. Goss, P. R. Briddon, and M. G. Wardle, Multi-impurity complexes for n-type diamond: A computational study, Phys. Status Solidi (a) 204, 2971 (2007).
- [50] T. Umeda, K. Watanabe, H. Hara, H. Sumiya, S. Onoda, A. Uedono, I. Chuprina, P. Siyushev, F. Jelezko, J. Wrachtrup, and J. Isoya, Negatively charged boron vacancy center in diamond, Phys. Rev. B 105, 165201 (2022).
- [51] X. Gonze, A brief introduction to the ABINIT software package, Z. Kristallogr. Cryst. Mater. 220, 558 (2005).
- [52] M. Torrent, F. Jollet, F. Bottin, G. Zérah, and X. Gonze, Implementation of the projector augmented-wave method in the ABINIT code: Application to the study of iron under pressure, Comput. Mater. Sci. 42, 337 (2008).
- [53] X. Gonze et al., ABINIT: First-principles approach to material and nanosystem properties, Comput. Phys. Commun. 180, 2582 (2009). 40 YEARS OF CPC: A celebratory issue focused on quality software for high performance, grid and novel computing architectures.
- [54] X. Gonze et al., Recent developments in the ABINIT software package, Comput. Phys. Commun. 205, 106 (2016).
- [55] N. Bindzus, T. Straasø, N. Wahlberg, J. Becker, L. Bjerg, N. Lock, A.-C. Dippel, and B. B. Iversen, Experimental determination of core electron deformation in diamond, Acta Crystallogr. A 70, 39 (2014).
- [56] A. Cammarata, M. Kaintz, and T. Polcar, Engineering width and directness of the band gap in diamond-based materials: An ab initio investigation towards electronstructure features control, Diam. Relat. Mater. 128, 109237 (2022).
- [57] Z. Wu and R. E. Cohen, More accurate generalized gradient approximation for solids, Phys. Rev. B 73, 235116 (2006).
- [58] H. J. Monkhorst and J. D. Pack, Special points for Brillouin-zone integrations, Phys. Rev. B 13, 5188 (1976).
- [59] S. Gao, Band gaps and dielectric functions of cubic and hexagonal diamond polytypes calculated by manybody perturbation theory, Phys. Status Solidi (b) 252, 235 (2014).
- [60] F. Belviso et al., Viewpoint: Atomic-scale design protocols toward energy, electronic, catalysis, and sensing applications, Inorg. Chem. 58, 14939 (2019).
- [61] J. Heyd, G. E. Scuseria, and M. Ernzerhof, Hybrid functionals based on a screened Coulomb potential, J. Chem. Phys. 118, 8207 (2003).
- [62] J. Heyd, G. E. Scuseria, and M. Ernzerhof, Erratum: "Hybrid functionals based on a screened Coulomb potential" [J. Chem. Phys. 118, 8207 (2003)], J. Chem. Phys. 124, 219906 (2006).
- [63] A. V. Krukau, O. A. Vydrov, A. F. Izmaylov, and G. E. Scuseria, Influence of the exchange screening parameter on the performance of screened hybrid functionals, J. Chem. Phys. **125**, 224106 (2006).

- [64] W. Hu, Z. Li, J. Yang, and J. Hou, Nondecaying long range effect of surface decoration on the charge state of NV center in diamond, J. Chem. Phys. 138, 034702 (2013).
- [65] D. E. Vanpoucke and K. Haenen, Revisiting the neutral C-vacancy in diamond: Localization of electrons through DFT + U, Diam. Relat. Mater. 79, 60 (2017).
- [66] A. Gali, M. Fyta, and E. Kaxiras, *Ab initio* supercell calculations on nitrogen-vacancy center in diamond: Electronic structure and hyperfine tensors, Phys. Rev. B 77, 155206 (2008).
- [67] E. G. Seebauer and M. C. Kratzer, Charged point defects in semiconductors, Mater. Sci. Eng. R-Reports **55**, 57 (2006).
- [68] O. D. Tucker, M. E. Newton, and J. M. Baker, EPR and ¹⁴n electron-nuclear double-resonance measurements on the ionized nearest-neighbor dinitrogen center in diamond, Phys. Rev. B **50**, 15586 (1994).
- [69] M. Muruganathan and H. Mizuta, Boron vacancy color center in diamond: Ab initio study, Diam. Relat. Mater. 114, 108341 (2021).
- [70] M. E. Bathen and L. Vines, Manipulating singlephoton emission from point defects in diamond and silicon carbide, Adv. Quantum Technol. 4, 2100003 (2021).
- [71] S. Kirklin, B. Meredig, and C. Wolverton, Highthroughput computational screening of new Li-ion battery anode materials, Adv. Energy Mater. 3, 252 (2013).
- [72] A. A. Emery and C. Wolverton, High-throughput DFT calculations of formation energy, stability and oxygen vacancy formation energy of ABO₃ perovskites, Sci. Data 4, 170153 (2017).
- [73] M. Roth, Y. Toker, and D. T. Major, Monte Carlosimulated annealing and machine learning-based funneled approach for finding the global minimum structure of molecular clusters, ACS Omega 9, 1298 (2024).
- [74] A. R. Oganov and C. W. Glass, Crystal structure prediction using *ab initio* evolutionary techniques: Principles and applications, J. Chem. Phys. **124**, 244704 (2006).
- [75] C. Freysoldt, B. Grabowski, T. Hickel, J. Neugebauer, G. Kresse, A. Janotti, and C. G. Van de Walle, Firstprinciples calculations for point defects in solids, Rev. Mod. Phys. 86, 253 (2014).
- [76] D. Zhang, X. Sun, Y. Zhang, C. Cheng, Y. Guo, Z. Gan, S. Liu, and Y. Hao, Theoretical study of n-type diamond with Li doping and Li-B co-doping: A density functional simulation, Diam. Relat. Mater. 131, 109544 (2023).
- [77] N. Gao, L. Gao, and H. Yu, First-principles study of N and S co-doping in diamond, Diam. Relat. Mater. 132, 109651 (2023).
- [78] Y. Makino, T. Mahiko, M. Liu, A. Tsurui, T. Yoshikawa, S. Nagamachi, S. Tanaka, K. Hokamoto, M. Ashida, M. Fujiwara, N. Mizuochi, and M. Nishikawa, Straightforward synthesis of silicon vacancy (SiV) center-containing single-digit nanometer nanodiamonds via detonation process, Diam. Relat. Mater. 112, 108248 (2021).
- [79] N. C. Murphy, R. Wortis, and W. A. Atkinson, Generalized inverse participation ratio as a possible measure of localization for interacting systems, Phys. Rev. B **83**, 184206 (2011).

- [80] D. Neamen, Semiconductor Physics And Devices (McGraw-Hill, Inc., USA, 2002), 3rd ed.
- [81] W. Setyawan and S. Curtarolo, High-throughput electronic band structure calculations: Challenges and tools, Comput. Mater. Sci. 49, 299 (2010).
- [82] See the Supplemental Material at http://link.aps.org/supple mental/10.1103/PhysRevApplied.23.054029 for generalized band gaps as a function of the defect concentration for all the defects and the electronic band structures calculated at 1.85% concentration along the standard piecewise linear path joining the high-symmetry points in the irreducible Brillouin zone of the face-centered cubic lattice. We also report the band dispersion of the structures doped with a single-dopant atom for comparison. The Supplemental Material also contains Refs. [56,81].
- [83] F. L. Hirshfeld, Bonded-atom fragments for describing molecular charge densities, Theor. Chim. Acta 44, 129 (1977).
- [84] A. Cammarata and J. M. Rondinelli, Covalent dependence of octahedral rotations in orthorhombic perovskite oxides, J. Chem. Phys. 141, 114704 (2014).
- [85] M. J. Han, C. A. Marianetti, and A. J. Millis, Chemical control of orbital polarization in artificially structured transition-metal oxides: La_2NiXO_6 (X = B, Al, Ga, In) from first principles, Phys. Rev. B **82**, 134408 (2010).
- [86] A. Cammarata and J. M. Rondinelli, Octahedral engineering of orbital polarizations in charge transfer oxides, Phys. Rev. B 87, 155135 (2013).
- [87] A. Cammarata and T. Polcar, Electro-vibrational coupling effects on "intrinsic friction" in transition metal dichalcogenides, RSC Adv. 5, 106809 (2015).
- [88] A. Cammarata and T. Polcar, Layering effects on low frequency modes in *n*-layered MX₂ transition metal dichalcogenides, Phys. Chem. Chem. Phys. **18**, 4807 (2016).
- [89] A. Gali and J. R. Maze, *Ab initio* study of the split silicon-vacancy defect in diamond: Electronic structure and related properties, *Phys. Rev. B* **88**, 235205 (2013).
- [90] J. Goss, R. Lowery, P. Briddon, and M. Rayson, Density functional theory study of Al, Ga and in impurities in diamond, Diam. Relat. Mater. **142**, 110811 (2024).
- [91] L. Muechler, D. I. Badrtdinov, A. Hampel, J. Cano, M. Rösner, and C. E. Dreyer, Quantum embedding methods for correlated excited states of point defects: Case studies and challenges, Phys. Rev. B 105, 235104 (2022).
- [92] K. Czelej, M. R. Zemła, P. Kamińska, P. Śpiewak, and K. J. Kurzydłowski, Clustering of hydrogen, phosphorus, and vacancies in diamond: A density functional theory analysis, Phys. Rev. B 98, 075208 (2018).
- [93] S. Salustro, G. Sansone, C. M. Zicovich-Wilson, Y. Noël, L. Maschio, and R. Dovesi, The A-center defect in diamond: Quantum mechanical characterization through the infrared spectrum, Phys. Chem. Chem. Phys. 19, 14478 (2017).
- [94] G. Brunin, F. Ricci, V.-A. Ha, G.-M. Rignanese, and G. Hautier, Transparent conducting materials discovery using high-throughput computing, npj Comput. Mater. 5, 63 (2019).
- [95] M. Moreira, J. Afonso, J. Crepelliere, D. Lenoble, and P. Lunca-Popa, A review on the p-type transparent Cu-Cr-O delafossite materials, J. Mater. Sci. 57, 3114 (2022).

- [96] P. Ashcheulov, A. Taylor, Z. Vlčková Zivcová, P. Hubík, J. Honolka, M. Vondráček, M. Remzová, J. Kopeček, L. Klimša, J. Lorinčik, M. Davydova, Z. Remeš, M. Kohout, A. Beltran, and V. Mortet, Low temperature synthesis of transparent conductive boron doped diamond films for optoelectronic applications: Role of hydrogen on the electrical properties, Appl. Mater. Today 19, 100633 (2020).
- [97] N. Wächter, C. Munson, R. Jarošová, I. Berkun, T. Hogan, R. C. Rocha-Filho, and G. M. Swain, Structure, electronic properties, and electrochemical behavior of a boron-doped diamond/quartz optically transparent electrode, ACS Appl. Mater. Interfaces 8, 28325 (2016).
- [98] J. V. Macpherson, A practical guide to using boron doped diamond in electrochemical research, Phys. Chem. Chem. Phys. 17, 2935 (2015).
- [99] R. Cao, H.-X. Deng, and J.-W. Luo, Design principles of p-type transparent conductive materials, ACS Appl. Mater. Interfaces 11, 24837 (2019).
- [100] D. O. Scanlon, J. Buckeridge, C. R. A. Catlow, and G. W. Watson, Understanding doping anomalies in degenerate p-type semiconductor LaCuOSe, J. Mater. Chem. C 2, 3429 (2014).
- [101] J. Zhang, J. Willis, Z. Yang, X. Lian, W. Chen, L.-S. Wang, X. Xu, T.-L. Lee, L. Chen, D. O. Scanlon, and K. H. Zhang, Deep UV transparent conductive oxide thin films realized through degenerately doped wide-bandgap gallium oxide, Cell Rep. Phys. Sci. 3, 100801 (2022).
- [102] A. K. Jonscher, The physics of the tunnel diode, Br. J. Appl. Phys. **12**, 654 (1961).
- [103] J. Copeland, Heavily-doped semiconductor lasers, IEEE J. Quantum Electron. 17, 2187 (1981).
- [104] K. S. A. Butcher and D. G. Alexandrov, Light emitting device using super-luminescence in semiconductor layer grown with Moss-Burstein effect (2014), International Patent Application PCT/AU2014/000113.
- [105] A. Walsh, J. L. F. Da Silva, and S.-H. Wei, Origins of band-gap renormalization in degenerately doped semiconductors, Phys. Rev. B 78, 075211 (2008).
- [106] V.-A. Ha, D. Waroquiers, G.-M. Rignanese, and G. Hautier, Influence of the "second gap" on the transparency of transparent conducting oxides: An *ab initio* study, Appl. Phys. Lett. **108**, 201902 (2016).
- [107] M. Sobaszek, L. Skowroński, R. Bogdanowicz, K. Siuzdak, A. Cirocka, P. Zieba, M. Gnyba, M. Naparty, L. Goluński, and P. Plotka, Optical and electrical properties of ultrathin transparent nanocrystalline boron-doped diamond electrodes, Opt. Mater. 42, 24 (2015).
- [108] W. Shockley and H. J. Queisser, Detailed balance limit of efficiency of *p-n* junction solar cells, J. Appl. Phys. **32**, 510 (1961).
- [109] A. Luque and A. Martí, Increasing the efficiency of ideal solar cells by photon induced transitions at intermediate levels, Phys. Rev. Lett. 78, 5014 (1997).
- [110] A. S. Brown and M. A. Green, Impurity photovoltaic effect: Fundamental energy conversion efficiency limits, J. Appl. Phys. 92, 1329 (2002).

- [111] I. Ramiro and A. Martí, Intermediate band solar cells: Present and future, Prog. Photovolt.: Res. Appl. 29, 705 (2021)
- [112] I. Ramiro, A. Martí, E. Antolín, and A. Luque, Review of experimental results related to the operation of intermediate band solar cells, IEEE J. Photovolt. 4, 736 (2014).
- [113] M. Rasukkannu, D. Velauthapillai, and P. Vajeeston, Computational modeling of novel bulk materials for the intermediate-band solar cells, ACS Omega 2, 1454 (2017).
- [114] G. Chen, H. Qiu, P. N. Prasad, and X. Chen, Upconversion nanoparticles: Design, nanochemistry, and applications in theranostics, Chem. Rev. 114, 5161 (2014).
- [115] Q.-C. Sun, Y. C. Ding, D. M. Sagar, and P. Nagpal, Photon upconversion towards applications in energy conversion and bioimaging, Prog. Surf. Sci. 92, 281 (2017).
- [116] N. López, K. M. Yu, T. Tanaka, and W. Walukiewicz, Multicolor electroluminescence from intermediate band solar cell structures, Adv. Energy Mater. 6, 1501820 (2016).
- [117] M. Wełna, M. Baranowski, W. Linhart, R. Kudrawiec, K. Yu, M. Mayer, and W. Walukiewicz, Multicolor emission from intermediate band semiconductor $ZnO_{1-x}Se_x$, Sci. Rep. 7, 44214 (2017).
- [118] F. Hatami, W. T. Masselink, and J. S. Harris, Colour-tunable light-emitting diodes based on InP/GaP nanostructures, Nanotechnology 17, 3703 (2006).
- [119] M. Y. Levy and C. Honsberg, Intraband absorption in solar cells with an intermediate band, J. Appl. Phys. 104, 113103 (2008).
- [120] M. Dandin, P. Abshire, and E. Smela, Optical filtering technologies for integrated fluorescence sensors, Lab Chip 7, 955 (2007).
- [121] J. Zhang, K. Tse, M. Wong, Y. Zhang, and J. Zhu, A brief review of co-doping, Front. Phys. 11, 117405 (2016).
- [122] I. Stenger, M.-A. Pinault-Thaury, T. Kociniewski, A. Lusson, E. Chikoidze, F. Jomard, Y. Dumont, J. Chevallier, and J. Barjon, Impurity-to-band activation energy in phosphorus doped diamond, J. Appl. Phys. 114, 073711 (2013).
- [123] J. Pernot, P. N. Volpe, F. Omnès, P. Muret, V. Mortet, K. Haenen, and T. Teraji, Hall hole mobility in boron-doped homoepitaxial diamond, Phys. Rev. B 81, 205203 (2010).
- [124] Y. M. Hongchao Yang and Y. Dai, Progress of structural and electronic properties of diamond: A mini review, Funct. Diam. 1, 150 (2021).
- [125] S. Shen, W. Shen, S. Liu, H. Li, Y. Chen, and H. Qi, First-principles calculations of co-doping impurities in diamond, Mater. Today Commun. 23, 100847 (2020).
- [126] K. Fan, K. Tang, M. Zhang, K. Wu, G. Zhao, Y. Huang, S. Zhu, J. Ye, and S. Gu, The boron-phosphorous co-doping scheme for possible n-type diamond from first principles, Comput. Mater. Sci. 222, 112113 (2023).
- [127] Y. Wu, J. Tong, L. Ruan, F. Luo, G. Liu, R. Zhang, X. Han, Y. Zhang, F. Tian, and X. Zhang, N-type diamond semiconductor induced by co-doping selenium and boron, Comput. Mater. Sci. 196, 110515 (2021).